International Journal of Plasticity 199 (2026) 104640

Contents lists available at ScienceDirect

International Journal of Plasticity

journal homepage: www.elsevier.com/locate/ijplas

Interface thickness size effects on strength and shear localizations in Cu/Nb nanolaminates

Mauricio De Leo [a,*,1], Nicolas Fuchs-Lynch [b,1], Justin Y. Cheng [a], Shuozhi Xu [c], Irene J. Beyerlein [b,d], Nathan A. Mara [a]

[a] Department of Chemical Engineering and Materials Science, University of Minnesota Twin Cities, Minneapolis, 55455, MN, USA
[b] Materials Department, University of California, Santa Barbara, 93106-5050, CA, USA
[c] School of Aerospace and Mechanical Engineering, University of Oklahoma, Norman, 73019, OK, USA
[d] Department of Mechanical Engineering, University of California, Santa Barbara, 93106-5070, CA, USA

ARTICLE INFO

Keywords:
Cu/Nb nanolaminates
Shear localization
3D interfaces
PFDD
Interface-driven strengthening

ABSTRACT

Bimetallic nanolaminates are exceptionally strong but suffer from a low strain to failure. Nanolaminates with unusually thick, "3D interfaces" (3DIs) have been shown to exhibit improvements in both properties. In this work, we investigate the strength and failure of Cu/Nb nanolaminates varying in individual layer thickness and 3D interface thickness. We show via *in situ* micropillar compression, nanoindentation, and post-mortem TEM that the mechanical property benefits of these thick interfaces persist over a relatively large space of layer and interfacial thicknesses. Within this range, the layer size effect on strength is weak or non-existent and deformation is delocalized and diffuse compared to the same nanolaminate with sharp interfaces. We present a phase field dislocation dynamics model to treat dislocations moving in a multi-phase FCC/BCC nanolaminate with a chemically and structurally gradient 3DIs. The effects of 3DI thickness on critical slip transfer stress to pass to/from the Cu and Nb layers and its dependence on slip direction (asymmetry) are aligned with trends in the measured strength and deformation, implying that the 3DI affects mechanical behavior by altering dislocation transmission. Our results showcase the two influential length scales controlling nanolaminate strength and failure-layer and interfacial thicknesses and suggests how they can be altered for improved performance in FCC/BCC Cu/Nb nanolaminates.

1. Introduction

Metallic nanolaminates are periodic stacks of immiscible metals with nanometer-scale periodicity, and exhibit exceptional mechanical strength, radiation tolerance, shock resistance, and thermal stability (Beyerlein et al., 2022; Wang et al., 2017; Hattar et al., 2008; Li et al., 2019; Nizolek et al., 2017; Zhang et al., 2024). These attributes make them attractive for a variety of applications, including energy-storage media and micro-electromechanical systems (Nasim et al., 2020; Ebrahimi et al., 2024; Qiu et al., 2012; Sim et al., 2017). Nanolaminate strength has two outstanding characteristics: it often far exceeds a volume averaged strength of its constituents and their strength increases as the individual layer thickness (h) reduces (Sáenz-Trevizo and Hodge, 2020; Zhang et al., 2017; Pathak et al., 2017; Chen et al., 2020a). The main concern with nanolaminates is their higher propensity and greater ease of shear localization with finer h. Nanolaminates often fail due to sudden formation of shear bands once the material

* Corresponding author.
E-mail address: trevi083@umn.edu (M. De Leo).
[1] M. De Leo and N. Fuchs-Lynch contributed equally to this work.

https://doi.org/10.1016/j.ijplas.2026.104640
Received 22 October 2025; Received in revised form 5 February 2026
Available online 11 February 2026

can no longer accommodate the strain uniformly (Gola et al., 2019). Plastic deformation is almost entirely carried by a single, highly localized shear band, leading to abrupt softening at a small global strain (Cao et al., 2019; Mara et al., 2010, 2008). These strength and failure characteristics are exhibited by many immiscible two—phase systems, including FCC/BCC, FCC/FCC, and HCP/BCC combinations. Among nanolaminates, FCC/BCC systems have been extensively studied and as such their interface structures and mechanical properties are well-defined. The Cu/Nb FCC/BCC system is the focus here.

Dislocation transmission across biphase interfaces was originally proposed as the mechanism underlying the superior strength of nanolaminates over conventional coarse-layered laminates (Hunter et al., 2018; Koehler, 1970). Stacking fault energy differences at the interface lead to a force due to a change in the energy of a stacking fault in a dissociated, transmitting dislocation, which results in a "blocking" stress. According to the analytical model, the interface only serves as a barrier when the dislocation transmits to the phase with the higher stacking fault energy. The proposed critical stress scales directly with the difference in stacking fault energy between the two materials. A greater slip plane misorientation, for instance, can lead to an increase in the interface barrier stress, due to the larger energy penalty from the larger magnitude residual dislocation left at the interface (Rao and Hazzledine, 2000; Lim and Raj, 1985). Additionally, the lattice parameter mismatch generates either coherency stresses for coherent interfaces or misfit dislocations for incoherent interfaces, either of which can interact with incoming dislocations attempting to transfer. Analytical models consider the contribution of one property difference between the two phases, enabling the ability to isolate its effect. Atomistic simulations consider all differences coupled together to affect dislocation transmission but this can make identifying their individual role challenging. Both methods treat slip transmission in one direction. At an intermediate length and time scale, a computational mesoscale modeling technique, called phase field dislocation dynamics (PFDD), has been used to investigate slip transfer across cube-on-cube FCC/FCC biphase interfaces accounting for coherency stresses, residual Burgers vector penalty, and moduli mismatch (Koehler stresses) (Zeng et al., 2016). The PFDD study showed that dislocations can face a barrier to slip transmission in both slip directions. However, the critical slip transfer stress is unequal and displayed an asymmetry, which follows:

$$\tau_{crit} \approx \frac{a_{(2)}\mu_{(2)}}{a_{(1)}+a_{(2)}}\left(\frac{a_{(1)}}{a_{(2)}}-\frac{\mu_{(1)}}{\mu_{(2)}}\right)^2 \tag{1}$$

where $a_{(1)}$ and $\mu_{(1)}$ are the lattice parameter and shear modulus for the material in which the dislocation originated and $a^{(2)}$ and $\mu^{(2)}$ for the material to which the dislocation transfers. The model predicts that the asymmetry with respect to slip transfer direction increases as both the difference in lattice parameter and elastic moduli increase.

In addition to the barrier effect supplied by the interface, the high strength of nanolaminates derives partly from the nanometer thick layers h that constrain dislocation processes and interface structure. Fine nanometer h can limit the sizes of dislocation nucleation sources, the expansion of dislocations, and the spacing between dislocations within pile ups. The material near or within the interface can assume metastable crystal structures (Demkowicz and Beyerlein, 2020). These constraints also influence failure in many multilayer systems. The failure strain, crack propagation, and flow localization of the brittle SiC phase can be dramatically altered when embedded within a layered Al/SiC composite laminates (Yang et al., 2020). A similar delay in the onset of failure and overall increase in ductility can be seen in tensile tests for martensitic/austenitic laminates (Singh and Jonnalagadda, 2024).

These aforementioned experimental, analytical, and simulation studies of dislocation transmission rationalize the effects of phase properties and processes and their relative differences across the interface on slip transfer. They often do not consider changing the interface properties itself, while keeping the phase properties and orientation fixed. In recent work, Cu/Nb in particular has been extensively studied and even been processed to create thick "3D" interfaces (3DIs) (Chen et al., 2020b; Cheng et al., 2022; Li et al., 2023; Selimov et al., 2022). A 3DI is an extended interfacial zone whose defining feature is its graded nature between the parent layers. The first micropillar test studies on a 50/50 Cu/Nb nanolaminate with h = 40 nm layers and 10 nm thick 3DIs hinted at the possibility that they can achieve even better mechanical performance than the same h = 40 nm Cu/Nb nanolaminate with a sharp (referred to as 2D) interface while simultaneously maintaining the same level of deformability (Chen et al., 2020b; Cheng et al., 2024). Further, the mode of shear banding in Cu/Nb nanolaminates becomes diffuse with wide shear bands that propagate in a stable manner.

While proving to lead to superior properties in a few Cu/Nb architectures, the mechanisms and reasons 3DIs have these effects have yet to be clarified. The original motivation behind 3D interfaces concerns their effect on dislocation transmission. Specifically, the hypotheses are that 3DIs discourage the formation of misfit dislocations by spreading the changes in lattice misfit over a larger distance and increase the critical stress for slip transfer by increasing the activation distance (Cheng et al., 2024; Selimov et al., 2022). These notions presume the dislocation can glide through the 3D interface and hence implicitly that the 3D interface remains crystalline and ordered through its thickness with a net composition of the two phases it joins. However, combined HR-TEM and ATP studies of a 10 nm 3D interface in Cu/Nb system revealed that certain areas of the 3DI contain amorphous precipitates, a few nanometers in dimension (Li et al., 2023). 3DI nanolaminates also add a second length scale that can potentially affect strength, the thickness of the 3DI (h')–in addition to the pure layer thickness of the individual layers (h). Insight into h' size effects is essential for identifying the limits of 3DI interface strengthening, to further investigate the parameters under which strengthening occurs, and for harnessing 3DIs effectively in design. Yet to date, no prior Cu/Nb 3DI experimental study has not analyzed such effects.

Experimental estimates of slip transfer are challenging if not impossible and the PFDD model has been employed to address the hypothesis concerning the effect of h' on dislocation slip transfer. In prior studies, a range of 3DI h' in either FCC/FCC or BCC/BCC nanolaminates were simulated (Xu et al., 2022a; Cheng et al., 2022). The calculations for both crystalline systems suggested that thicker 3DIs lead to higher critical transmission stresses, although once the 3DI is sufficiently thick, the strengthening enhancements remain constant. When the 3DI thickness h' and stacking fault width were similar, the critical stress reached a maximum. This finding

Table 1
Sample series with varying interface and layer thicknesses.

Series	Configurations ($h - h'$)
Series 1 (Constant h' = 10 nm)	80-10, 20-10, 10-10
Series 2 (Constant h = 10 nm)	10-40, 10-20, 10-10
Series 3 (Constant h/h' = 1)	40-40, 20-20, 10-10

is consistent with the analytical model by Hirsch and Kelly (1965), as well as with PFDD predictions for the stress required for a Ni dislocation to bypass a row of shearable precipitates (Zeng et al., 2019). As the 3DI h' increases, the mechanical advantage of the pile up becomes less effective, implying the relative stress to pass the lead dislocation in the pile-up increases (Xu et al., 2022b,a). Although insightful, the layers in the model were the same material, which prevents study of the effects of mismatches in moduli, lattice, and crystallographic orientation. The assumption also disables examination of the effects of h' on asymmetry in critical stress with respect to slip transfer direction. To date, size effects of h' on strength have not been studied experimentally or computationally in any FCC/BCC system. Perhaps more importantly it limits the insight gained from comparisons, albeit qualitative, with experimentally measured strengths on Cu/Nb nanolaminates.

In this work, we investigate a broad range of Cu/Nb nanolaminates with independently varied h and 3DI h' to establish how interface dimensions influence mechanical behavior. In—situ micropillar compression tests coupled with ex—situ electron microscopy are used to measure strength and directly observe yield and deformation patterns, including shear localization characteristics as h and h' are analyzed. With the constraint effects in mind, in the systems that will be studied here, nanolaminates with and without 3D interfaces with the same h are compared. The structure of the 3D interfaces are consistent with the equilibrium crystal structure based on their chemical composition. Last, we focus on the size effects on the plastic response and leave fracture to future studies. The experimental results attempt to identify a window for h and h' for where strength and deformability are high in interface-rich nanolaminates.

To gain insight into underlying dislocation mechanisms at the nanoscale, we incorporate computational PFDD modeling of dislocation transfer to/from Cu and Nb layers across 3D interfaces of different thicknesses and compositional and structural gradients. The PFDD results indicate that increases in 3D interface thicknesses increase the slip transfer critical stress and reduce its dependence on slip transfer direction. Qualitatively, the former finding is consistent with the experimental measurements of yield strength and flow stresses at higher strain levels.

2. Methods

2.1. Nanolaminate synthesis, morphological, and nanomechanical characterization

Cu/Nb nanolaminates were synthesized using an AJA Orion Hybrid PVD DC Magnetron Sputtering system at the Center for Integrated Nanotechnologies (CINT) at Los Alamos National Laboratory. Deposition was performed on Si (100) substrates with a native oxide layer. The base pressure during deposition was maintained in the low 10^{-7} Torr range, ensuring high purity in the deposited films. The 3DIs were achieved by linearly modulating the sputtering power to the Cu and Nb targets to co-sputter both constituents. 10 μm thin films with various h and h' on single crystal Si substrates were deposited. Additionally a 10 μm thick amorphous equiatomic CuNb sample was deposited at a deposition rate of 3 Å/sec by using a continuous Cu target power of 75 W and Nb target power of 200 W. The samples deposited for this work are displayed in Table 1.

In order to characterize the morphology of the nanolaminates, focused ion beam (FIB) was conducted in a FEI G4 Helios FIB/SEM at an acceleration voltage ranging from 30 kV to 1 kV, with the voltage lowered as the sample was thinned, to prepare TEM foils. Morphological characterization via conventional TEM (CTEM), high-resolution TEM (HRTEM) and scanning TEM energy dispersive spectroscopy (STEM-EDS) were performed with a Thermo Fisher Talos F200X at 200 kV, equipped with a Super-X G2 EDX detector. The bilayer thicknesses for each sample in Table 1 were measured across 10 bilayers and 3 lateral positions, then dividing the averages and standard deviations by 10 to measure the average bilayer thickness.

Nanoindentation tests were conducted using a Hysitron TI 980 nanoindenter equipped with a standard transducer with a maximum load capacity of 12 mN and a Berkovich tip. The tip area function was calibrated up to 600 nm on a fused silica standard, with calibration data confirming agreement with known hardness values. Continuous stiffness measurement (CSM) tests were performed at 100 Hz, with a displacement amplitude of 1–2 nm.

Micropillar compression was performed for deformability analysis. A final current of 1 nÅ was used to mill micropillars with an aspect ratio (height divided by diameter) of about 2. The methodology is explained in detail in Jiang and Chawla (2010). Uniaxial compression was applied to pillars at an initial strain rate of 1×10^{-3} s^{-1} in a Bruker/Hysitron PI-85 in-situ SEM straining stage.

A constant strain rate profile was applied during the dynamic contact (DC) phase, with an indentation strain rate of 5×10^{-3} s^{-1} between 10 and 300 mN. Each test lasted 360 s, with data acquired at 100 points per second. Ten indents were performed per specimen, spaced 75 μm apart. To minimize thermal drift effects, specimens were placed in the nanoindenter enclosure for 1 h before testing. A thermal drift settling segment was executed before each indent, lasting 100 s or until the drift rate fell below 0.500 nm/s, whichever occurred first.

All stress–strain curves in this study employ engineering stress and strain. Stress was calculated using the diameter at the top of the pillar, representing the maximum engineering stress in the sample. Strain was determined based on gage length, following the methods in Cheng et al. (2022).

A separate methodology was necessary due to the varying degrees of shear localization among samples. In some cases, shear localization occurred before the pillar taper model predicted the transition to a right cylinder, violating its underlying geometric assumptions. Consequently, true stress and strain calculations, which assume volume conservation and cylindrical geometry, could not be applied. Shear localization disrupts uniaxial stress conditions, rendering true stress–strain calculations invalid. Therefore, engineering stress–strain curves were chosen to ensure consistent comparison across all samples in this study.

2.2. PFDD formulation

PFDD is the modeling method we adopt for this study. This method simulates dislocation configurations and their motion in crystals (Beyerlein and Hunter, 2016; Xu et al., 2020b). PFDD is well suited for this study on 3DIs as it accounts for the details of the dislocation core structure as it changes with crystal structure, moduli and composition, while being able to treat long dislocation lengths and multiple interacting dislocations. The necessary atomic-scale inputs are only the anisotropic stiffness tensor and γ-surfaces, which can be determined from MD or, in the case in which interatomic potentials are not available, a DFT calculation. The simulation evolves by minimizing its free energy, containing the elastic energy, generalized stacking fault energy, and work done. This minimization is performed at every time step (Mianroodi and Svendsen, 2015; Roach et al., 2023) to predict the dislocation configuration.

The PFDD model used here is the multi-phase version, formulated to determine dislocation motion in a material system composed of multiple phases of different crystal structures, with differing elastic moduli and γ-surfaces. For the present case, the only material properties needed for input are the lattice constants, the full elastic stiffness tensor, and the generalized stacking fault energies (GSFE) for the relevant slip planes. The GSFE values are taken from DFT calculations, previously reported for pure Cu and Nb (Xu et al., 2020,a), while properties of the 3DI for the Cu-Nb alloys are taken from Xu et al. (2022c). As in the experiment, the Cu and Nb crystals follow the Kurdjumov-Sachs orientation relationship. Here, PFDD simulations are carried out for the two directions of slip transfer and for both one and two dislocations along the predominant, well aligned $\{110\}\langle 111\rangle$ Nb – $\{111\}\langle 110\rangle$ Cu slip system pathway. The analysis focuses on the effect of 3DI thickness h' and pure layer thickness h on the critical slip transfer stress and its path dependence. Accordingly, the phase where the dislocation initially lies, the layer thickness, and 3DI thickness will be varied in the model. The present formulation of PFDD adopts the small strain assumption. It is employed to obtain insight into the role of the interface thickness on the critical slip transfer stress of one or a few dislocations. As such slip transfer of so few dislocations involves small strains and no lattice rotations, justifying use of the small strain assumption.

PFDD models a discretized 3D system, in which the free energy of every point evolves in space and time as a function of scalar-valued order parameters. Each order parameter ϕ^α represents the position of dislocation slip in the slip system α. One order parameter is associated with slip by a single slip system. An order parameter $\phi^\alpha = N$ corresponds to a region that has been slipped N times, whereas $\phi^\alpha = 0$ represents an region that is unslipped (Beyerlein and Hunter, 2016; Mianroodi and Svendsen, 2015.)

In order to evolve the system, the following contributions are used to calculate the total free energy at each timestep:

$$\psi(x) = \psi_{ela}(x) + \psi_{lat}(x) - \psi_{ext}(x) \tag{2}$$

Here, $\psi_{ela}(x)$ accounts for the elastic strain energy as a result of the dislocation and dislocation-dislocation interactions, $\psi_{ext}(x)$ is due to the work done by the dislocation as a result of the applied stress, and $\psi_{lat}(x)$ represents the energy due to dislocation motion through the lattice, where atomic bonds are broken and reformed. Usually a gradient term is added in general phase field formulations, which serves to regularize the width of the interface. In PFDD, the width is associated with the size of the dislocation core. The elastic stiffness will regularize the width of the core and with the gradient energy term omitted, the width of the interface is still finite. Nevertheless, the gradient energy term has been included in the energy function in prior works (Wang and Li, 2010; Xu et al., 2019; Mianroodi and Svendsen, 2015). In these studies, the gradient term coefficient was shown to modify the width of the partial dislocation cores and affect the stacking fault width in a second order manner. Core structures from atomistic calculations can be used to identify this coefficient for a range of FCC metals (Roach et al., 2023). Among the pure FCC metals, the coefficient for Cu was the smallest, nearly zero. Thus, the gradient term is not included in the total free energy for Cu.

Here we present the extension of the PFDD formulation to treat heterogeneous media, consisting of N_{mat} materials containing different elastic moduli (Lei et al., 2013; Xu et al., 2022c,b). The modification incorporates the idea of an eigenstrain introduced by Eshelby (1957). In order to characterize the elastic energy density, the eigenstrain tensor ϵ^0 is first defined as:

$$\boldsymbol{\epsilon}^0(x) = \begin{cases} \boldsymbol{\epsilon}^p(x), & x \in \text{material } 1 \\ \boldsymbol{\epsilon}^p(x) + \boldsymbol{\epsilon}^v(x), & x \in \text{material } N \text{ in regions with dislocations } (N \neq 1) \\ \boldsymbol{\epsilon}^v(x), & x \in \text{material } N \text{ without dislocations } (N \neq 1) \end{cases} \tag{3}$$

with $\boldsymbol{\epsilon}^v$ representing the virtual strain tensor, which comes about due to the moduli mismatch.

The plastic strain tensor $\boldsymbol{\epsilon}^p$ has the following relation to the plastic distortion tensor $\boldsymbol{\beta}^p$ and the order parameter ϕ_α:

$$\boldsymbol{\epsilon}^p = sym\boldsymbol{\beta}^p \tag{4}$$

Above, sym represents the symmetric part of the tensor.

$$\boldsymbol{\beta}^p(\phi) = \sum_{\alpha=1}^{n_{op}} \frac{b^\alpha \phi^\alpha}{d^\alpha}\, \boldsymbol{s}^\alpha \otimes \boldsymbol{n}^\alpha \tag{5}$$

Here, s^α is the slip direction unit vector, b^α represents the Burgers vector magnitude, n^α is the normal to the slip plane, and d^α is the interplanar spacing between adjacent slip planes for slip system α.

$\psi_{ela}(x)$ accounts for the elastic energy density of the homogeneous medium, denoted $\psi^{eq}_{ela}(x)$, and the additional elastic energy density $\psi^{ex}_{ela}(x)$ of the inhomogeneities, such that:

$$\psi_{ela}(x) = \psi^{eq}_{ela}(x) + \psi^{ex}_{ela}(x) \tag{6}$$

with

$$\psi^{eq}_{ela}(x) = \frac{1}{2}\,[\boldsymbol{\epsilon}(x) - \boldsymbol{\epsilon}^0(x)] \cdot \boldsymbol{C}[\boldsymbol{\epsilon}(x) - \boldsymbol{\epsilon}^0(x)] \tag{7}$$

where $\epsilon_0(x)$ is defined in Eq. (3).

$$\psi^{ex}_{ela}(x) = \frac{1}{2}\,\boldsymbol{\epsilon}^v(x) \cdot \boldsymbol{M}^{[N]}(x)\boldsymbol{\epsilon}^v(x) \tag{8}$$

Here, $\boldsymbol{C}$ is the elasticity tensor, $\boldsymbol{\epsilon} = sym(\boldsymbol{\beta})$ is the strain tensor, $\boldsymbol{\beta} = \nabla \boldsymbol{u}$ is the distortion, and $\boldsymbol{u}$ is the displacement. For a material $1 < N \leq N_{mat}$:

$$M^{[N]}_{ijkl}(x) = -C^{[1]}_{ijmn}[\Delta C^{[N]}_{mnpq}(x)]^{-1}C^{[1]}_{pqkl} - C^{[1]}_{ijkl} \tag{9}$$

$$\Delta C^{[N]}_{ijkl}(x) = C^{[N]}_{ijkl}(x) - C^{[1]}_{ijkl} \tag{10}$$

The virtual strain is present in all materials except for material 1. While the elastic moduli are homogeneous, the virtual strain fields are generally inhomogeneous for each phase.

ψ_{lat}, the lattice energy density, can be represented as

$$\psi_{lat}(x) = \frac{\gamma^{[N]}_{gsf}(\phi(x))}{l^{[N]}_{gsf}} \tag{11}$$

Here $\gamma^{[N]}_{gsf}$ is the GSFE represented as a function of the order parameter ψ for material N and $l^{[N]}_{gsf}$ is the interplanar spacing between slip planes on which the GSFE is determined for material N.

We express ψ_{ext}, the external energy density, as follows:

$$\psi_{ext}(x) = \boldsymbol{\sigma}_{app}\boldsymbol{\epsilon}^0(x) \tag{12}$$

where $\boldsymbol{\sigma}_{app}$ is the stress tensor corresponding to the applied stress.

The total system energy is minimized at each timestep with respect to each order parameter ψ_α and the virtual strain components $\boldsymbol{\epsilon}_{ij}$ according to the time-dependent Ginzburg–Landau (TDGL) equations, shown below:

$$\dot{\phi}^\alpha(x) = -m[\partial_{\phi_\alpha(x)}(\psi_{ela}(x) + \psi_{lat}(x) - \psi_{ext}(x))] \tag{13}$$

$$\dot{\boldsymbol{\epsilon}}^v_{ij}(x) = -m^v \frac{\partial \psi}{\partial \boldsymbol{\epsilon}^v_{ij}} \tag{14}$$

Here, m and m^v are relaxation coefficients. These non-negative constants determine the rate of convergence to the equilibrium. Constant relaxation coefficients are chosen to ensure that the configuration and virtual strain converge in every time step. We find that setting these values to unity leads to convergence, since the equilibrium state is unaffected by their values (Zeng et al., 2016).

2.2.1. Formulation for simulating amorphous precipitates

Here we consider the case where portions of the 3D interface may be amorphous. The current PFDD model represents the motion of discrete dislocations, which are defined as precise imperfections in a crystalline structure. Therefore, dislocations can exist and glide in the crystalline phases but not in the amorphous ones. If we let material M, designate the amorphous phase, ϕ are the order parameters in all materials besides material M. The lattice energy density for an amorphous material $\psi_{lat}(x) = 0$. The external energy density $\psi_{ext}(x) = \boldsymbol{\sigma}_{app} \cdot \boldsymbol{\epsilon}^v(x)$. The elastic energy density for the amorphous material is only a function of the virtual strain $\boldsymbol{\epsilon^v}(\boldsymbol{x})$ and not the order parameter ϕ.

$$\psi_{ela}(x) = \psi^{ex}_{ela}(\boldsymbol{\epsilon^v}(\boldsymbol{x})), x \in \text{material M} \tag{15}$$

In material M where dislocations cannot glide the system evolves according to Eq. (14), whereas in the crystalline materials $2 - N$ where dislocations can glide, the system evolves according to both equations (13) and (14).

Table 2
Lattice parameters a_0 (in Å), elastic constants C_{11}, C_{12}, C_{44} (in GPa), Isotropic shear modulus in Voigt form $\mu = \frac{3C_{44}+C_{11}-C_{12}}{5}$ (in GPa), Isotropic Poisson's ratio in Voigt form $\nu = \frac{(C_{11}+4C_{12}-2C_{44})}{(4C_{11}+6C_{12}+2C_{44})}$, γ_{usf} (in mJ/m^2), and Burgers vector value (in Å).

Material	a_0	C_{11}	C_{12}	C_{44}	μ	ν	γ_{usf}	b
Nb	3.324	245	132	28.40	39.64	0.392	676.78	2.879
$Cu_{0.1}Nb_{0.9}$	3.274	221.58	141.63	40.63	40.37	0.389	703.46	2.835
$Cu_{0.5}Nb_{0.5}$		193.70	135.90	30.80	30.04	0.409		
$Cu_{0.8}Nb_{0.2}$	3.759	195.16	128.44	79.32	60.94	0.322	463.52	2.658
Cu	3.634	169	122	75.30	54.58	0.325	519.05	2.570

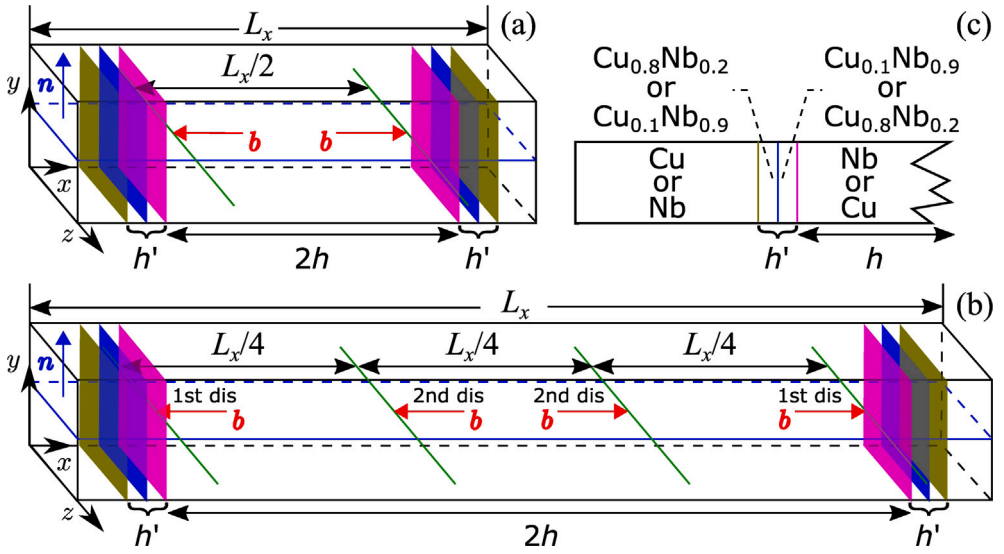

Fig. 1. Simulation cell for edge dislocations interacting with two 3DIs. For each 3DI, there are (a) one or (b) two dislocation dipoles.

2.3. Material input

The layers consist of BCC Nb and FCC Cu while the 3DIs consist of BCC $Cu_{0.1}Nb_{0.9}$ and FCC $Cu_{0.8}Nb_{0.2}$ and in the case where amorphous precipitates are modeled, the precipitates are $Cu_{0.5}Nb_{0.5}$. As mentioned, in the PFDD model, important material parameters include the lattice parameter a_0, elastic constants C_{11}, C_{12}, and C_{44}, and the GSFE curves. The (110) and (111) planes are set as the common glide plane in BCC and FCC materials, respectively. In $Cu_{0.1}Nb_{0.9}$ and $Cu_{0.8}Nb_{0.2}$, respectively, 20 GSFE curves are calculated using 20 random atomic structures, following Xu et al. (2020a), and the median GSFE curve is considered here. In each material, the peak value of a GSFE curve is the unstable stacking fault energy (USFE), γ_{usf}. Note that in BCC and FCC materials, respectively, the GSFE curve is along the $\langle 111 \rangle$ and $\langle 110 \rangle$ directions. Values of all material parameters used in this work are summarized in Table 1. Values of a_0 and γ_{usf} in Nb and Cu are obtained from prior density functional theory (DFT) calculations (Xu et al., 2020). The values of C_{11}, C_{12}, and C_{44} in Nb and Cu are taken from experiments (Warlimont and Martienssen, 2018). All values in $Cu_{0.1}Nb_{0.9}$, $Cu_{0.8}Nb_{0.2}$, and $Cu_{0.5}Nb_{0.5}$ are given by atomistic simulations (Xu et al., 2022b). More details of the multi-phase PFDD model can be found in Ref. Xu et al. (2022c,a).

The simulated dislocations are undissociated. This is a good approximation for edge dislocations in Nb, but may not be indicative of the edge dislocations in Cu. Prior PFDD work which considered a full FCC nanolaminate with an FCC 3DI led to the conclusion that slip transfer of dissociated dislocations in Cu can contribute to the effect of h' on slip transfer, specifically when the width of the core is larger than h' (Xu et al., 2022a). However, in this study, the cores of Cu and Nb are presumed to be much narrower than the values of h' considered. The focus is on determining the 3DI size effects, which remain significant for thicknesses larger than the core width of the dislocations.

2.4. Simulation setup

As illustrated in Fig. 1, one or two dislocation dipoles are inserted into a 3D periodic simulation cell. Each dipole contains two edge dislocations with opposite Burgers vectors. The crystallographic orientations are x$\langle 111 \rangle$, y$\langle 110 \rangle$, and z$\langle 112 \rangle$.

In each cell, all dislocations lie on the mid-y plane and are equi-distanced. Two 3DIs are respectively located on the mid-y plane. Let L_x, L_y, and L_z be the edge length of the simulation cell along the x, y, and z directions, respectively. In all cases, $L_y \approx 15$ nm and $L_z \approx 35$ nm, while $L_x > 2(h + h')$, where h and h' are the layer thickness and 3DI thickness, respectively. In the case h $\geq h'$,

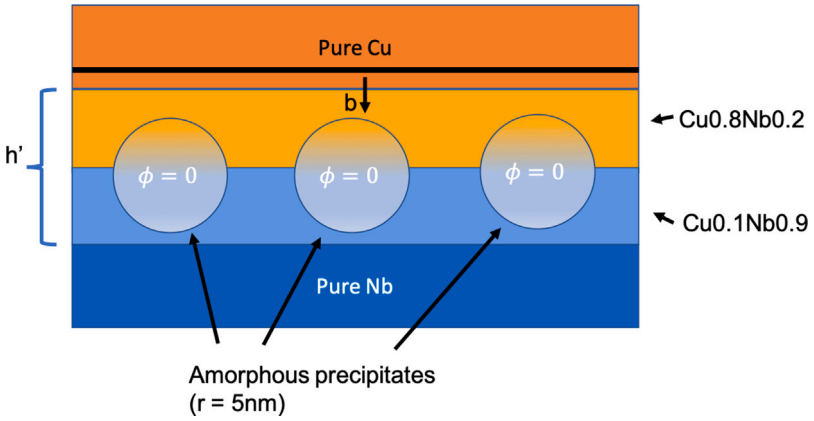

Fig. 2. Schematic of PFDD simulation cell setup with amorphous precipitates present in the 3D interface.

h is either 10 nm or 40 nm, while h' is either 10 nm, 20 nm, or 40 nm. Simulations containing two 2D interfaces (i.e., $h' = 0$ nm) are also conducted to provide references. In each case, the dislocation may be initiated in Cu and then move to Nb, or the reverse configuration. Following Xu et al. (2022b,a,c), an incremental resolved shear stress (RSS) is applied to the system, until the edge dislocation begins to transmit through the entire 3DI. The minimum stress needed for complete transmission of the full dislocation from one layer, across the interface, and into the next layer is considered the critical stress. In the cases of two dislocations in the same pile-up, after the transmission of the first dislocation, however, it may be that the second dislocation cannot transmit through the 3DI under the same RSS. The RSS must then be incremented further until the next dislocation can fully transmit. Thus, in the case of two dislocations in the pile up, it is possible that two critical stresses can be obtained for each 3DI thickness, one to permit the first to fully transmit and another for the second to fully transmit.

To model the amorphous region seen in 3DIs in experiment, slip transfer simulations are performed with the same 3DI approximation with the addition of three amorphous $Cu_{0.5}Nb_{0.5}$ precipitates of 5 nm diameter in the center of the 3DI. The spacing between the precipitates is 4 nm. The precipitates are centered in the middle of the 3DI. In simulations with differing h' values, these precipitates have the same dimension and remain in the center of the interface. A schematic of this setup can be seen in Fig. 2. The properties used to simulate the amorphous can be seen in Table 2, specifically the precipitates are assumed to have composition of Cu0.5Nb0.5. The dislocation must bow through the precipitates and cannot slice through them, since dislocations cannot exist in an amorphous material.

3. Results

3.0.1. Layer-to-interface thickness dependency on deformation behavior

We first investigate the relative influence of the interface and layer thicknesses on the mechanical behavior of the 3DI nanolaminates by analyzing the changes in strength with the ratio h/h'. As a reference, we include strengths for the sharp interface (2D) nanolaminates $h' = 0$ and for metallic glass, which theoretically corresponds to a material composed of only 3D interface material ($h' = \infty$). Fig. 3 shows the micropillar compression flow stress of all 3DI samples plotted against their h/h' ratio. The total layer plus interface thicknesses $(h + h')$ tested in these samples are ≤ 100 nm. Nanolaminates with $(h + h') \leq 50$ nm (or $h/h' \leq 4$) exhibit an ultra high strength that is relatively insensitive to h/h'. These properties are much higher than that of the metallic glass, corresponding to $h/h' = 0$ on this plot. For the same h, the strengths are much higher than those of the 2D nanolaminates (shown versus h on the upper x-axis since $h' = 0$). As h/h' increases further, the strength of the 3D nanolaminates drops significantly and nearly coincides with that of the 2D nanolaminates for the same value of h. Evidently, there is a limit to 3DI strengthening, when the pure metal layer thickness h exceeds that of the 3DI thickness by 8 times.

Fig. 3 suggests a crossover in interface 3DI effects as a function of h/h', around $h/h' \approx 4$. As mentioned earlier, nanolaminates derive their strength from the constraint on dislocation processes that increases as h decreases, such as confining pile up lengths, as well as increased participation of the interface on these processes as its density increases as h decreases. With relatively thick 3DIs, i.e., low h/h', it is posited that the constraint and interface effects are coupled, such that slip transfer of very few dislocations across the 3DI controls strength, rendering strength nearly independent of h/h'.

This proposition puts forth a strong implication that selectively controlling the thickness of the pure layer h and 3DI h' leads to selective deformation modes. Post-mortem TEM data on 3DI containing samples showcased in Fig. 3 suggests that 3DI modify the formation, propagation and thickness of shear bands in Cu/Nb. As seen in Fig. 5, the shear band in $(h - h')$ 10-10 Cu/Nb is significantly wider than in the 40-10 Cu/Nb, where there is a pronounced localization of strain. From our select experimental matrix, narrower pure layers from nanolaminates containing 3DIs trend toward facilitating early shear band formation, resulting in broader and less confined shear bands. This higher resistance to localized deformation provides more volume where strain can accommodate uniformly, resulting in greater deformability at higher strengths. Consequently, if the stress is concentrated along a broader region,

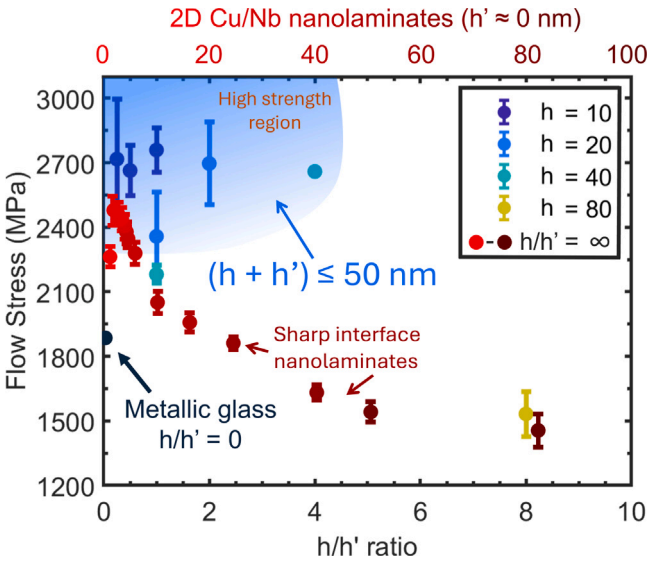

Fig. 3. Micropillar compression flow stress of nanolaminates with various combinations of $h + h'$. The sky blue region denotes a region where most combinations of $(h + h') \leq 50$ nm have superior strength than their sharp interface counterparts. The data suggests that specific layer and interface thicknesses combinations promote enhanced strength. The red spectrum data was extracted from Misra et al. (2005), involving only 2D interface Cu/Nb nanolaminates, which strength saturate in the lower high strength region at $h \approx 2$ nm. (For interpretation of the references to color in this figure legend, the reader is referred to the web version of this article.)

the material requires higher load inputs for shear band propagation. The following parameters were used in order to quantitatively measure the shear band severity. The layer-normal strain gradient, denoted as $\nabla\varepsilon_{\text{layer}}$, quantifies the spatial rate of change in layer thinning across a shear band and serves as an experimental metric for deformation localization severity in Cu/Nb nanolaminates. The layer-normal strain, $\varepsilon_{\text{layer}}$, is defined as the relative reduction in bilayer thickness measured normal to the locally rotated interface after shear deformation, expressed as

$$\varepsilon_{\text{layer}} = \frac{h_0 - h_d}{h_0} \tag{16}$$

where h_0 is the undeformed bilayer thickness and h_d is the deformed bilayer thickness measured perpendicular to the local interface orientation (Mara et al., 2010; Chen et al., 2020b). The strain gradient is then calculated as the difference in $\varepsilon_{\text{layer}}$ between two locations separated by a distance Δx along the shear band propagation direction:

$$\nabla\varepsilon_{\text{layer}} = \frac{\varepsilon_{\text{layer},a} - \varepsilon_{\text{layer},b}}{\Delta x} \tag{17}$$

Measurement locations were selected in regions exhibiting the most rapid change in $\varepsilon_{\text{layer}}$ to capture the local deformation gradient across the shear band. This metric enables quantitative comparison of strain localization severity across multilayer architectures with varying interface morphology. To visualize the methodology used for strain quantification, Fig. 4 illustrates the measurement of the layer-normal strain, $\varepsilon_{\text{layer}}$, and the corresponding strain gradient, $\nabla\varepsilon_{\text{layer}}$, across a shear band in a Cu/Nb nanolaminate.

Representative measurements of $\varepsilon_{\text{layer}}$ and $\nabla\varepsilon_{\text{layer}}$ were performed across shear bands in Cu/Nb nanolaminates with varied h and h'. Fig. 5 shows TEM images illustrating the local reduction in bilayer thickness within shear bands and the corresponding calculation of $\varepsilon_{\text{layer}}$ for each material system for direct comparison. Other microstructural metrics associated with shear banding such as lattice and interface rotation are summarized in Table 3.

The methodology followed to measure ε_{layer}, h_d and h_0 is the following: the measurements were performed by averaging two bilayer periods, and six h_d measurements were taken at each ε_{layer}, while h_0 was taken from the average bilayer thickness in Table 4, which was measured in the undeformed samples through an identical process. The Δx was taken by averaging thalf of the length of both of the measured ε_{layers}. The sample orientation is selected by choosing the Si substrate 110 zone axis of the substrate by diffraction pattern alignment, which can be tilted within $\pm 0.01°$ by holder readout, as these were all deposited on Si 100 with a native oxide layer, therefore ensuring the sample is perfectly aligned with such plane. To minimize the effects of stress relaxation in thin regions, our measurements are taken away from free surfaces and edges, and are made in lamella regions of uniform thickness as can be seen in Fig. 5. To minimize the effects of FIB damage, we do a low-KV final polish of 1 kV at 1.2 nA for 2 min per side.

The 3D Cu/Nb nanolaminates discussed in Fig. 3 represent a targeted set of 3DI-containing architectures designed to explore the influence of layer and interface thickness on strength and deformation behavior. The following sections detail the individual deformation characteristics of these nanolaminates, focusing on their distinct strength responses compared to other nanolaminates in their class and their mechanical behavior as different function combinations of h and h'.

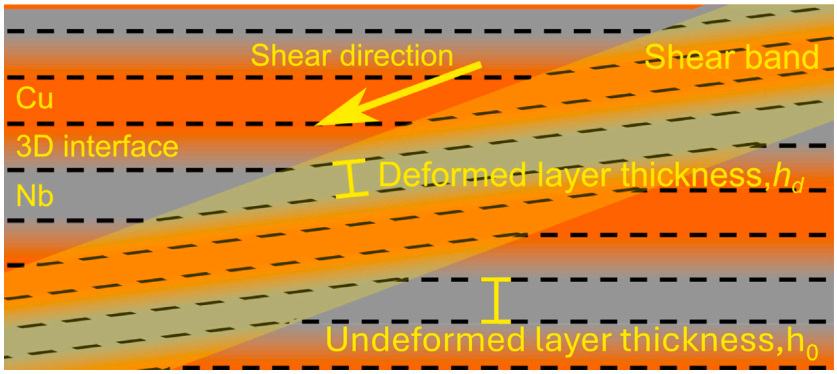

Fig. 4. Measurement of h_0 and h_d for calculating ϵ_{layer} and $\nabla\epsilon_{\text{layer}}$ across a shear band.

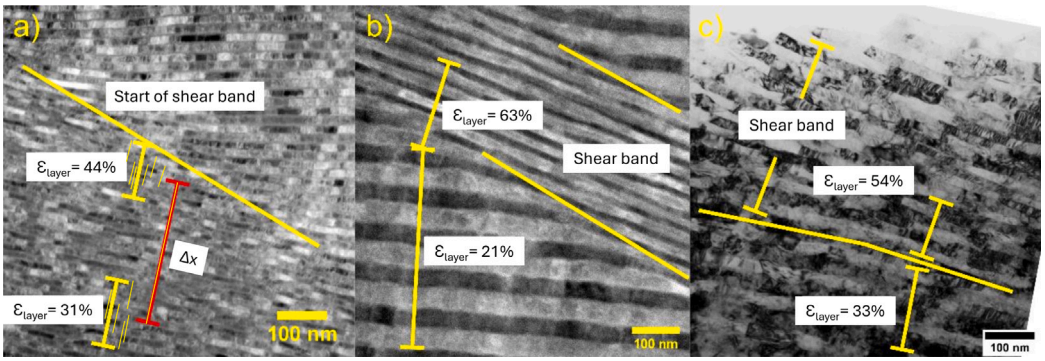

Fig. 5. Comparative shear band formation in different Cu/Nb nanolaminates. (a) 10-10 Cu/Nb broad shear band snapshot at 0.27 strain. Strain is accommodated over a large volume and the layer-to-layer change in strain happens gradually, as can be seen in the 10-10 stress–strain curve in Fig. 6(a), where the onset of plasticity occurs over a strain range. Small yellow lines in (a) denote measurement overlays performed through ImageJ for reasonable quantitative backing. (b) 40-10 Cu/Nb exhibits a narrower shear band, indicative of stress localization. (c) 2D 40 Cu/Nb. Shear band is found between the yellow lines. ϵ_{layer} is calculated both inside and outside the shear band as there is plastic deformation outside the shear band. The figure is adapted from Cheng et al. (2024). (For interpretation of the references to color in this figure legend, the reader is referred to the web version of this article.)

Table 3
Summary of shear band microstructural metrics from post-mortem TEM analysis among dissected Cu/Nb samples, were ϵ_{bulk} corresponds to the bulk engineering strain. The table shows a modified version of Table 4 in Cheng et al. (2024) with a corrected $\epsilon_{layer}/\epsilon_{bulk}$ for sample 40nm 2D Cu/Nb and measured inferface rotation.

Sample	ϵ_{bulk}	ϵ_{layer}	$\epsilon_{layer}/\epsilon_{bulk}$	$\nabla\epsilon_{layer}$	Lattice rotation	Interface rotation
10-10 3D Cu/Nb	0.16	0.44	2.75	0.045%/nm	31°	9.4°
40-10 3D Cu/Nb	0.14	0.63	4.5	0.13%/nm	30°	12°
40 nm 2D Cu/Nb	0.14	0.54	3.86	0.12%/nm	Not measured	17.5°

In order to properly assess with high accuracy how the parent layer and 3DI influence the mechanical properties, bilayer thickness was measured/verified by FIB cross-section and subsequent SEM and presented in Table 4. Note that the h/h′ ratio remains constant as the layer/interface ratios within the bilayer period deviate proportionally. Bilayer thicknesses were measured using FIB cross-sections followed by SEM analysis, as summarized in Table 4.

Most samples exhibited bilayer thicknesses within ĩ0% of their nominal values, except for 10–20 and 80-10 Cu/Nb, which measured approximately $5/6^{\text{ths}}$ of their intended thickness. Therefore, their nominal thickness values was used for subsequent analysis.

3.1. Mechanical sensitivity to h variation with constant h′

Micropillar compression results for 3D Cu/Nb with a fixed 3DI thickness (h' = 10 nm) are shown in Fig. 6. The stress–strain curves in Fig. 6(a) demonstrate that for pure layer thicknesses (h) up to 40 nm, flow stress remains relatively constant.

Table 4
Bilayer thickness measurements obtained from FIB cross-sections for samples listed in Table 1.

Sample	Nominal bilayer thickness (nm)	Average bilayer thickness ± STD (nm)	Percent error
10–10	40	42.8 ± 0.57	6.98%
10–20	60	50.0 ± 0.91	−16.69%
10–40	100	92.3 ± 0.88	−7.75%
20–10	60	57.5 ± 0.90	−4.13%
20–20	80	76.4 ± 0.60	−4.44%
40–40	160	142.0 ± 1.05	−11.27%
80–10	180	154.1 ± 1.71	−14.41%

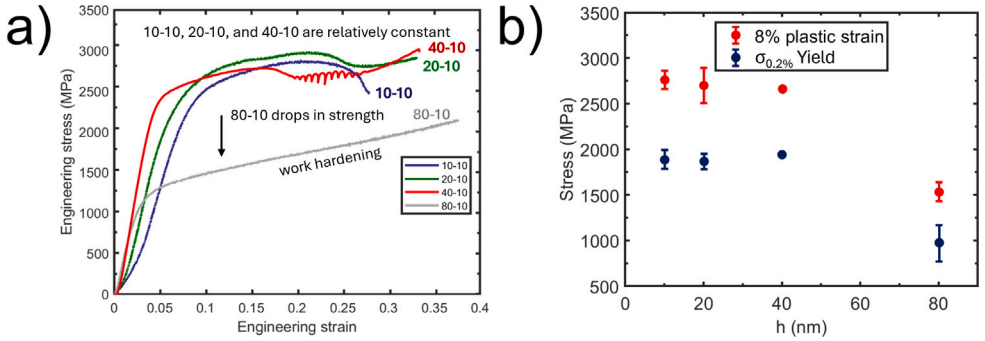

Fig. 6. (a) Engineering stress–strain curves for samples with h′ = 10 nm and varied h, showing a drop in yield strength as the pure layer thickness h surpasses 40 nm. Slight probe-pillar misalignment and small geometric differences from sample to sample, inherent of the FIB milling process introduce compliance in the loading curve and cause differences in the elastic moduli of the samples. (b) $\sigma_{8\%}$ and $\sigma_{0.2\%}$ presented as a function of h with h′ constant for samples in (a). Both yield ($\sigma_{0.2\%}$ and $\sigma_{8\%}$) are relatively constant from $h = 10 - 40$.

Further increasing h to 80 nm leads to a significant reduction in flow stress. This has been seen multiple times for this length scale (Zheng et al., 2014; Hoagland et al., 2002; Wang and Misra, 2011; Zhang et al., 2014). For samples with $h \leq 40$ nm, the onset of failure due to shear localization is seen in the form of stress drops at high plastic strain. In contrast, the 80-10 Cu/Nb sample exhibits global strain hardening, suggesting that work hardening in grain interiors counteracts shear band-induced softening. This behavior resembles the more uniform work hardening observed in coarser-grained alloys. The stress is reported at 8% true strain following a standing convention in micropillar tests and FE models for nanolaminates since they often have a gradual onset of full plasticity.

3.2. Mechanical sensitivity to h′ variation with constant h

3.2.1. h = 10 nm

In situ micropillar compression results for samples with a fixed pure layer thickness (h = 10 nm) are shown in Fig. 7. Fig. 7(a) presents representative stress–strain curves for all tested samples. Comparing 10-10 and 10–20 Cu/Nb shows that increasing the 3DI thickness (h') from 10 to 20 nm has little effect on flow stress. Both samples exhibit significant stress drops at high plastic strain, indicating nucleation of wide strain-softening shear bands that limit uniform deformation after significant strain. Increasing h' from 20 to 40 nm drastically changes the deformation mode. The 10–40 Cu/Nb sample reaches peak stress at a much lower strain than samples with smaller h'. 10–40 reached its peak stress at 0.10 strain, where the material undergoes a pronounced stress drop, followed by a relatively steady engineering stress up to a second stress drop at 0.30 strain. The shear localization behavior in 10–40 Cu/Nb will be examined further in Section 3.2.5. Fig. 7 (a) reflects how the plastic strain remains consistent through different 3DI thicknesses, and how the yield strength increases with 3DI thickness as has been seen for Cu/Nb in literature (Xu et al., 2022a).

3.2.2. h = 20 nm

In situ micropillar compression results for samples with a pure layer thickness of h = 20 nm are shown in Fig. 8. Slight peak stress local maximas can be seen in Fig. 8(a), and the stress drops after shear band formation are less pronounced. Both samples exhibit shear band formation at higher plastic strains than 10–40 Cu/Nb.

Fig. 8(b) shows that the yield stress $\sigma_{0.2\%}$ and flow stress at 8% plastic strain $\sigma_{8\%}$ are statistically comparable for both samples. Increasing the pure layer thickness to h = 20 nm improved deformability before shear band formation at thinner 3DI thicknesses h'. Both samples exhibit similar strain softening behavior, suggesting that these mechanical effects are more dependent on h for these h and h' length-scale regimes.

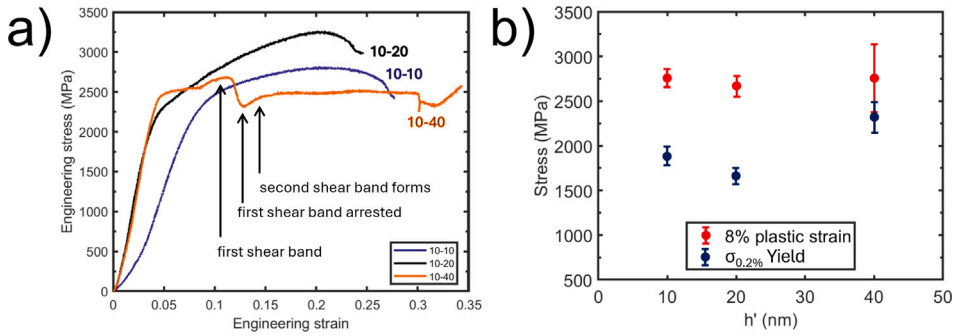

Fig. 7. Stress–strain behavior and post-mortem analysis of Cu/Nb micropillars with constant pure layer thickness of $h = 10$ nm. (a) Engineering stress strain-curves from samples with h = 10 nm and varied h'. (b) $\sigma_{8\%}$ and $\sigma_{0.2\%}$ presented as a function of h' with h constant for samples in (a). $\sigma_{8\%}$ is relatively constant from $h' = 10 - 40$, while yield stress $\sigma_{0.2\%}$ increases with increasing h'. (c) (i–ii) *In situ* micropillar compressions snapshots at the strains indicated by red dots in (a). (c) (i) shows the formation of one shear band that emanates from the pillar side at the yellow arrow. (c) (ii) shows the formation of a second shear band at the bottom of the pillar. (For interpretation of the references to color in this figure legend, the reader is referred to the web version of this article.)

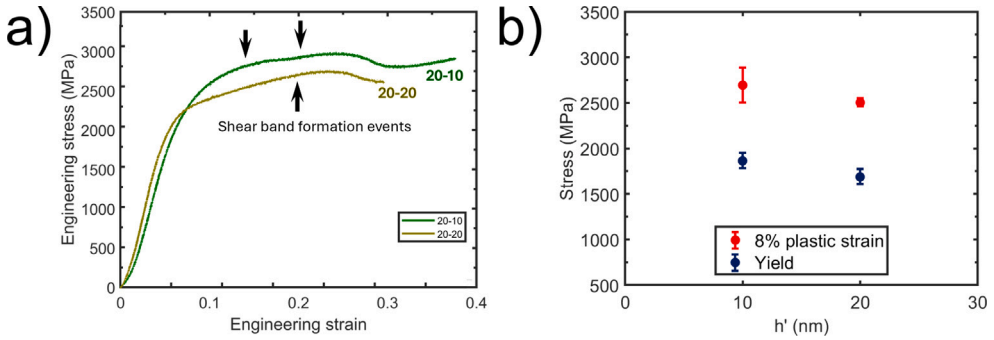

Fig. 8. Stress–strain behavior and post-mortem analysis of Cu/Nb micropillars with constant pure layer thickness of $h = 20$ nm. (a) Engineering stress vs. strain curves showing local stress maxima and shear band formation events (black arrows). (b) Yield stress $\sigma_{0.2\%}$ and flow stress $\sigma_{8\%}$ at 8% plastic strain for 20-10 and 20-20 Cu/Nb nanolaminates. (c–d) In situ snapshots at the end of pillar compression for (c) 20-10 Cu/Nb and (d) 20-20 Cu/Nb.

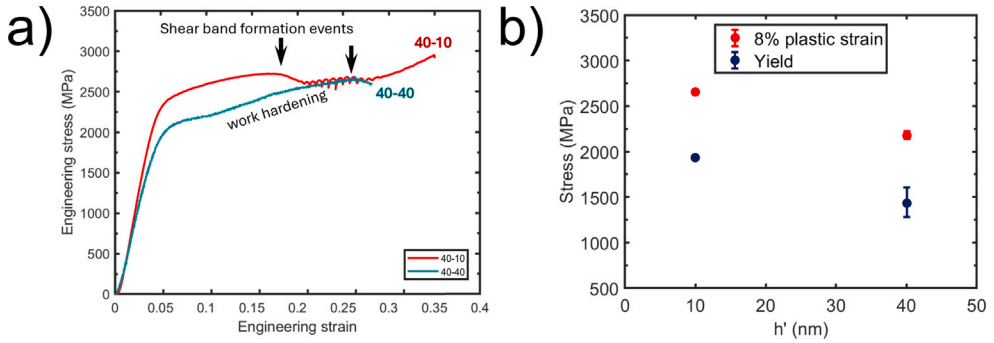

Fig. 9. Stress–strain behavior and post-mortem analysis of Cu/Nb micropillars with constant pure layer thickness of $h = 40$ nm. (a) Engineering stress vs. strain curves showing local shear band formation events (black arrows). (b) Yield stress $\sigma_{0.2\%}$ and flow stress $\sigma_{8\%}$ at 8% plastic strain for 40-10 and 40-40 Cu/Nb nanolaminates. (c–d) In situ snapshots at the end of pillar compression for (c) 40-10 Cu/Nb and (d) 40-40 Cu/Nb. (d) The snapshot is prior to shear localization, showing how the pillar bulges significantly before shear, in contrast to 40-10.

3.2.3. h = 40 nm

The results from micropillar compression displayed in Fig. 9 compare the micropillar compression behavior of 40-10 and 40-40 Cu/Nb. Thickening the 3D resulted in a lower yield strength, but delayed the onset of shear band formation, showing a more uniform deformation after yield. Both materials attain similar flow stresses before undergoing plastic instability.

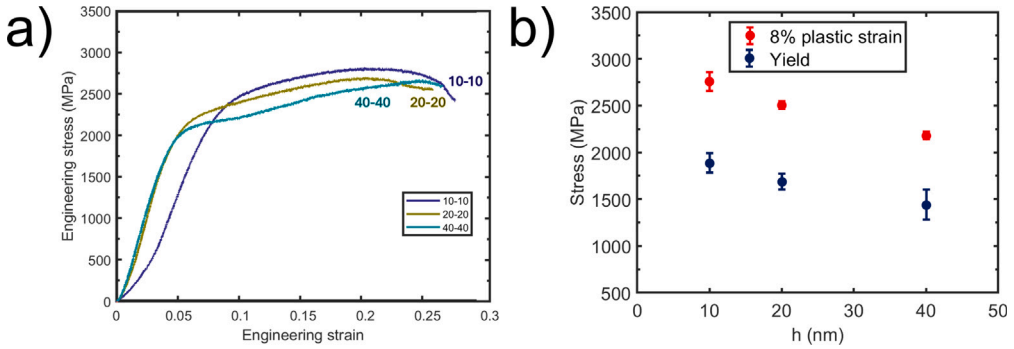

Fig. 10. (a) Stress–strain behavior of Cu/Nb micropillars with constant pure layer thickness to interface ratio $h/h' = 1$. (a) Engineering stress vs. strain curves showing an increase in yield stress without loss of deformability. (b) Yield stress $\sigma_{0.2\%}$ and flow stress $\sigma_{8\%}$ at 8% plastic strain for 10-10, 20-20, and 40-40 Cu/Nb nanolaminates.

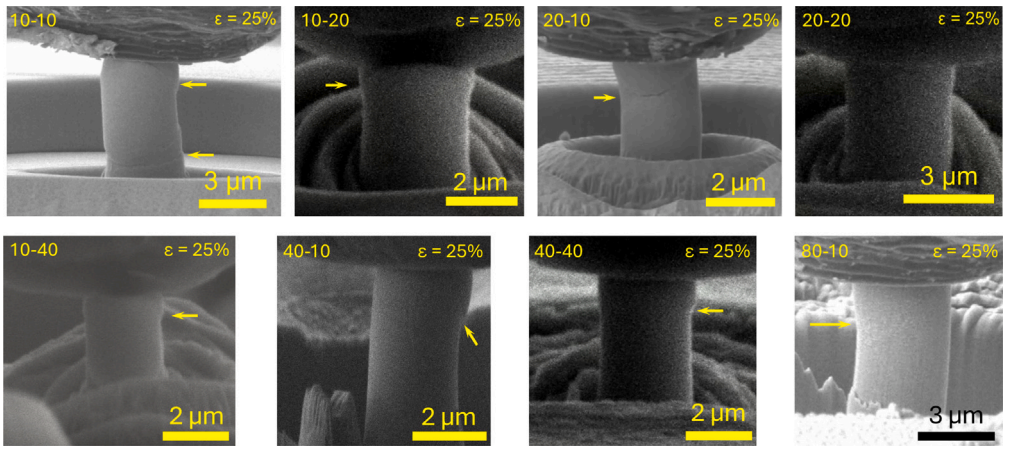

Fig. 11. Snapshots of the pillar compressions at $\varepsilon = 25\%$, which is a strain at which all the compression tests are past the onset of full plasticity. Multiple slip bands form in all pillars. See the supplementary information for videos of the compressions.

The 40-10 Cu/Nb sample reaches a maximum flow stress of approximately 2600 MPa before shear localization initiates at 0.15 strain; 40-40 Cu/Nb reaches a peak stress of approximately 2500 MPa at a higher strain of 0.23. There is a plastic instability after the shear band formation for 40-10, showing artificial small stress cycles between strains of 0.20–0.26. This is a plastic instability that our PI-85 transducer could not keep up with. Fig. 9(b) shows a strength drop going from $h' = 10$ to $h' = 40$, but it does not capture the post yield work-hardening behavior differences observed in 40-40 Cu/Nb beyond 8% plastic strain versus 40-10. This indicates that increasing the 3DI thickness from 10 to 40 improves the deformability and mechanical stability at higher plastic strains of nanolaminates.

3.2.4. *Constant* $h/h' = 1$

The effects of a constant layer-to-interface thickness ratio ($h/h' = 1$) were examined based on their bilayer thickness measurements as shown in Table 4. Fig. 10(a) shows that as h and h' increase while maintaining a constant h/h' ratio, flow stress decreases without an evident loss in deformability. The deformation behavior does change between 10-10 and 20-20, as the latter shows a more pronounced transition between the elastic and plastic components, which suggests a greater brittle-like behavior. Despite increasing strength, significant stress drops occur at a consistent total strain of 0.22. Given the similarity in elastic loading portions, this suggests that the plastic strain at which instability occurs remains unchanged.

Fig. 10(b) confirms the trend observed in Fig. 10(a), showing increasing flow stress with decreasing h and h'. The difference between yield stress (σ_y) and flow stress at 8% plastic strain ($\sigma_{8\%}$) remains consistent across all samples, and yield stress increases approximately linearly when both h and h' decrease. Since h represents the effective grain size of the material, this result suggests that decreasing h does not compromise work hardenability in the presence of 3DIs. This presents additional proof that 3DIs enable simultaneous strength enhancement and deformability retention, noticeably mitigating the conventional strength-deformability tradeoff. Fig. 11 shows a comparison among all samples showcased in this study, of their morphology and whether they have developed shear bands at $\varepsilon = 25\%$.

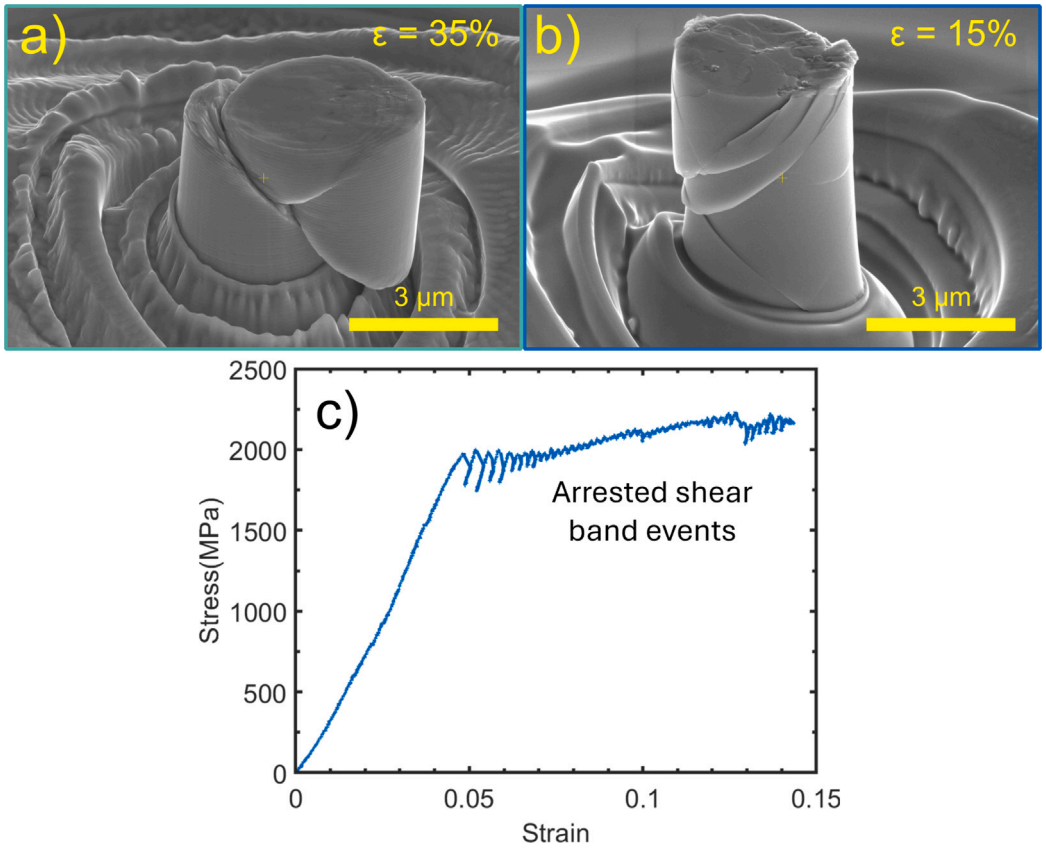

Fig. 12. Post-deformation SEM micrographs of (a) 10–40 Cu/Nb at 0.35 total strain and (b) cosputtered CuNb at 0.15 total strain. (c) Engineering stress–strain curve for the pillar shown in (b). The apparent load-unload behavior in the stress–strain curve in (c) is attributed to momentary loss of displacement control by the PI 88 control loop, a common occurrence during rapid load shedding in nanomechanical testing.

3.2.5. High h' Cu/Nb nanolaminate behavior vs. metallic glass CuNb

The interplay between nanolaminate architecture and amorphous-like behavior at large 3DI (h') thicknesses offers a fascinating contrast in mechanical performance. Fig. 12 captures the deformation behavior of 10–40 Cu/Nb nanolaminates and cosputtered equiatomic CuNb, illustrating how approximating h/h' ratios to zero increase shear localization and deformability, as it would be the case for metallic glasses..

In Fig. 12(a), 10–40 Cu/Nb, strained to 0.35 total strain, exhibits multiple shear bands distributed across the pillar width. While severe localization leads to rupture, the nanolaminate structure retains moderate deformability. The nanolaminate architecture allows strain to be redistributed more effectively, delaying catastrophic failure. The dominant shear band intersects with secondary ones, creating a complex failure mechanism that balances strength with some degree of ductility.

By contrast, Fig. 12(b) shows the behavior of amorphous equiatomic CuNb, where the theoretical $h/h' \rightarrow 0$ induces metallic glass-like properties. At 0.15 total strain, multiple arrested shear bands form, spanning a significant portion of the pillar width. These bands, characteristic of metallic glasses, are highly localized and unable to redistribute strain uniformly, leading to brittle rupture at much lower strains compared to the nanolaminate structure.

The stress–strain response of Fig. 12(b) is highlighted in 12(c). Amorphous CuNb exhibits continuous stress drops after the elastic region, corresponding to strain softening and displacement bursts associated with arrested shear bands. Such behavior, typical of metallic glasses (Geng et al., 2022; Ye et al., 2009; Yang et al., 2010), contrasts sharply with the gradual stress reduction and strain accommodation seen in 10–40 Cu/Nb.

These observations reveal a critical insight: as h' increases in Cu/Nb systems, the 3DIs transition from facilitating strain redistribution to adopting metallic glass-like behavior. While these interfaces can arrest shear bands, after a critical length-scale they sacrifice uniform deformability, resulting in brittle failure. Optimized h and h' thicknesses in nanolaminates like 10–40 Cu/Nb avoid the catastrophic localization observed in amorphous CuNb.

3.3. Computational calculation of lattice glide stresses

The experimentally observed deviations in mechanical response of 3D Cu/Nb do not directly capture the intrinsic stress scales governing dislocation motion within the individual layered phases. To bridge this gap, we next examine lattice glide stresses in Cu

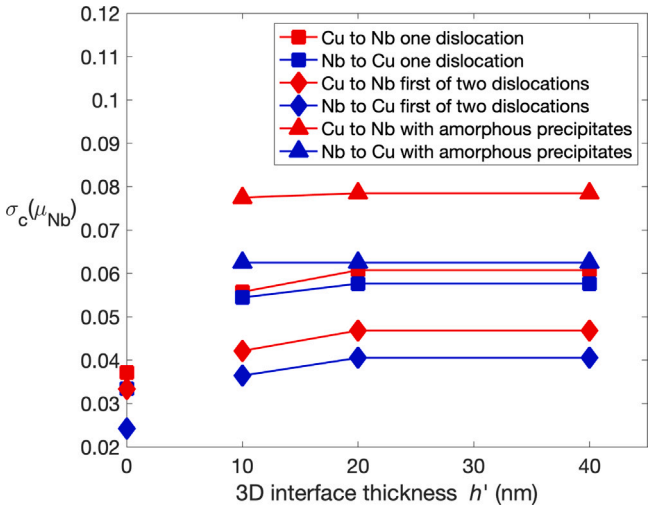

Fig. 13. Critical stresses for an edge dislocation starting in Cu (red) or Nb (blue). Squares indicate the critical stress for a single dislocation to undergo slip transfer, a diamond indicates the critical stress for the first of two dislocations in a pileup to undergo slip transfer, and a triangle indicates the critical stress for a single dislocation to undergo slip transfer with amorphous precipitates present in the 3DI. (For interpretation of the references to color in this figure legend, the reader is referred to the web version of this article.)

and Nb through PFDD calculations, providing a baseline for evaluating the role of 3DIs in modifying local deformation behavior. Specifically, we first estimate τ_0, the critical stress for an edge dislocation to glide in a given plane in either Cu or Nb (free of other phases). For τ_0, we calculate the minimum applied shear stress to initiate motion in a large crystal, free of interfaces. (This could also be referred to as a PFDD calculation of the lattice friction stress or a Peierls stress.) When expressed in μ_{Nb}, effective isotropic modulus of Nb, τ_0 are calculated to be $0.0335\mu_{Nb}$ and $0.00185\mu_{Nb}$ for the (110) Nb plane, and for the (111) Cu plane, respectively. Their differences reflect the fact that the peak of the GSFE is higher in Nb than Cu. These calculations are for undissociated dislocations and do not consider finite temperature effects, so we expect their values to be relatively high compared to room temperature experimental values. These critical glide stresses only serve as reference stresses to aid in comparisons between materials and systems and to help determine the effect of introducing the 3DI.

3.3.1. Critical slip transfer stresses

Next, we first examine the case where the dislocation originates in Nb and then glides into the BCC Nb-rich alloy, then the Cu-rich FCC alloy, and then finally into Cu, completing the transmission event. The relationship between the critical stress for slip transfer and h' can be seen in Fig. 13. Here, the critical stress for the 2D case, where neither alloy is present ($h' = 0$ nm), is the same as τ_0 for Nb. Hence, the Nb dislocation will glide across the interface with no additional stress required for slip transfer. This is reasonable, as there is a sharp decrease in USFE from 676.78 mJ/m^2 in Nb to 519.05 mJ/m^2 in Cu.

With increases in the interface thickness to 10 nm from the traditional 2D case, however, the critical stress required to cross the interface increases. The enhancement can be attributed to both the higher USFE of $Cu_{0.1}Nb_{0.9}$ (703.46 mJ/m^2) than pure Nb and the moduli mismatch when gliding into a stiffer material in shear. Upon increasing the thickness from 10 to 20 nm, we see only a moderate enhancement. While there is no change in the USFE landscape, the elastic differences become slightly more pronounced as the volume of stiffer material increases with greater h'. Beyond a critical h', thickening the interface does not result in additional increases in strength. The effect of elasticity differences between Nb and the stiffer 3DI and Cu have diminished.

Next, we analyze the reverse direction of slip transfer, from Cu to Nb. This can also be seen in Fig. 13. In this case, the 2D interface imposes a critical stress that is more than an order of magnitude higher than that which is required for glide in Cu alone. Based on analytical arguments for stacking fault effects, this is expected, as the dislocation is moving from a lower USFE region to one that is significantly larger. Once the interface is thickened, the critical stress nearly doubles, largely due to the introduction of a barrier with a larger change in USFE, namely from $Cu_{0.8}Nb_{0.2}$ to $Cu_{0.1}Nb_{0.9}$. These increases in strength continue up to 20 nm and then plateau. Thus, thickening the interface produces a stronger material for the Cu to Nb direction as well.

For both orientations, the cases where h' is kept fixed and h is varied were also tested. Changing h was found to not affect the critical stress for either initial dislocation configuration (when the number of dislocations was kept fixed). Since varying h does not change the structural or chemical properties of the 3DI layers but merely changes the extent to which the dislocation glides unhindered before reaching the interface, the lack of effect on the critical stress is expected. We discuss how well this correlates to the effect of h seen in experiment in the discussion.

For the simulations where two dislocations are present in a pileup, it is found that the critical stress for the first dislocation, i.e., the stress for the dislocation to first cross the 3DI, decreases due to the presence of the second dislocation. This reduction arises as a result of the repulsive force applied on the first dislocation by the second dislocation in the pile-up. More dislocations should

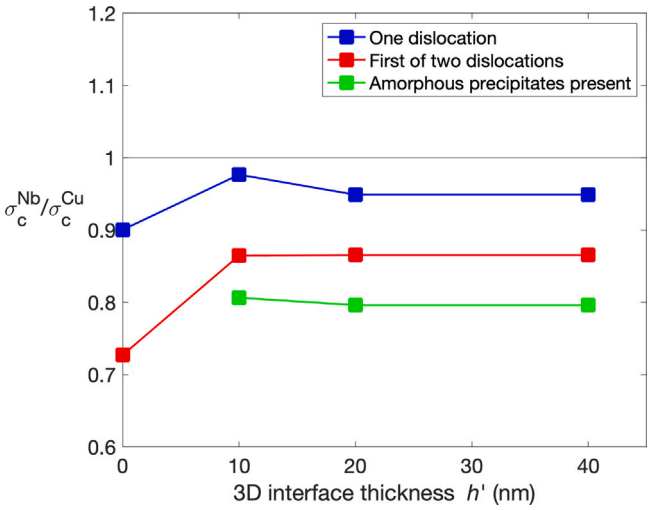

Fig. 14. Asymmetry ratio–the ratio of the critical stress for slip transfer for dislocations starting in Nb to dislocations starting in Cu for the case of one dislocation (blue), the first of two dislocations (red), or one dislocation with amorphous precipitates in the 3DI (green). (For interpretation of the references to color in this figure legend, the reader is referred to the web version of this article.)

be expected to lower the strengthening barrier of any interface. Yet the calculations show that compared to a sharp interface, the 3DI still is a stronger barrier in a two dislocation pile up and the thicker it is, the greater the transmission stress. The h' at which the strengthening plateaus for the first of two dislocations is the same as for a single dislocation. We may speculate that the positive size effect offered by the 3DI could manifest in nanolaminates with thicker h layers, containing larger dislocation pile ups.

Upon introduction of the $Cu_{0.5}Nb_{0.5}$ amorphous precipitates into the center of the 3DI, the critical stress for slip transfer increases for both slip transfer configurations. The critical stresses for slip transfer here are due to the energy penalty of slip transmission across the crystalline portions of the interface and bowing around the amorphous precipitates in the crystalline parts. The critical configuration for the case where the dislocation starts in Nb is when it starts to bow around the precipitates. On the other hand, when the dislocation starts in Cu, it has bowed much more around the precipitates. This trend is similar to that seen in 3DIs without the amorphous precipitates. The strengthening effect of amorphous precipitates has been predicted by simulation in other metallic nanolaminates (Ye et al., 2025). The size effect of the amorphous precipitates was not probed in this work, as a previous PFDD study (Xu et al., 2022c) showed that the critical stress will increase as the density of the precipitates increases.

Also notable is the lack of size effect in h'. As the h' increases, the size and spacing of the amorphous precipitates remained the same. This only further supports the notion that the amorphous precipitates dominate the resistance to dislocation motion. The exact increment depends on the spacing and size of the amorphous clusters. Here, only one configuration was tested to demonstrate and reveal its effect. There is, however, a greater increase compared to the case without amorphous precipitates when the dislocations originate in Cu. The more pronounced asymmetry between the two slip transfer pathways is not so clearly anticipated, since the arrangement of precipitates is symmetric about the interface plane.

Thus far, we have seen that the 3DIs more effectively resist transmission when dislocations in Cu transfer to Nb than in the reverse direction. The asymmetry can be more easily analyzed by plotting the slip transfer asymmetry ratio. Fig. 14 shows the ratio when starting in Nb to when starting in Cu as a function of h'. In all cases of layer pile ups and 3DI structure, the ratio remains less than unity. It is nearly equal to one (no asymmetry) for the case of one dislocation simulated. Further, the asymmetry ratio is closest to one for $h' = 10$ nm. When the amorphous precipitates are present within the 3DI, the slip transfer asymmetry is even further enhanced, where transmitting from Cu is harder than the reverse.

4. Discussion

4.1. Transition from interface dominance to bulk dominance

The mechanical response of Cu/Nb nanolaminates to varying interface thicknesses demonstrates a transition from interface-dominated strengthening to a regime where strain delocalization takes precedence. When keeping h' constant, strength remains high until a critical h somewhere between 40 and 80 nm, beyond which the bulk-like behavior begins to override interface effects, causing a drop in strength, unlike conventional 2D Cu/Nb nanolaminates where maximum strength is achieved at very fine layer thicknesses ($h < 5$ nm). The introduction of 3DIs extends the high-strength regime by increasing slip transfer resistance, effectively delaying the onset of bulk plasticity mechanisms.

A critical indicator of this transition lies in the observed Tabor factor evolution. The Tabor factor, which correlates hardness with uniaxial flow stress, presents a deviation from expected values ($2.7 - 3.0$), signaling a fundamental shift in how 3DIs influence

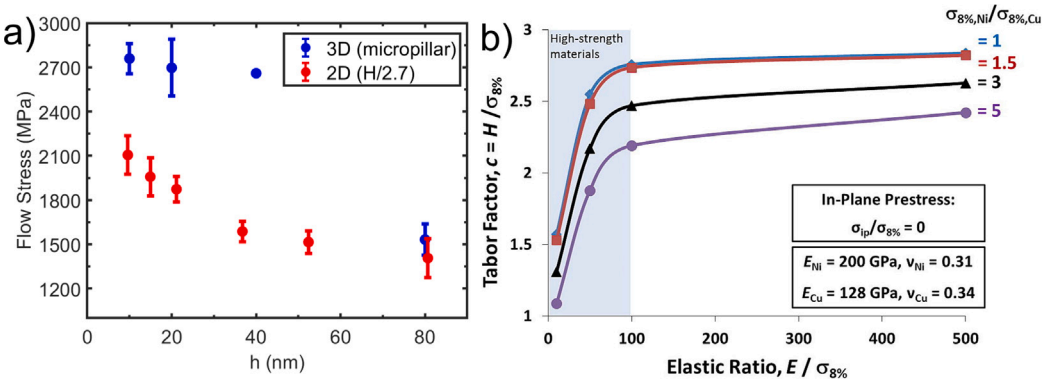

Fig. 15. (a) Comparison of flow stress between 3D Cu/Nb micropillar compression tests of nanolaminates with varying pure layer thickness h and 2D Cu/Nb nanohardness-based approximated flow stress with Tabor factor 2.7. (b) Dependence of the Tabor factor on flow strength at 8% plastic strain $\sigma_{8\%}$ and the flow strength ratio of constituent materials $\sigma_{8\%_A}/\sigma_{8\%_B}$ with zero prestress. Extracted from Gram et al. (2015), where a Ni/Cu system is analyzed.

stress distribution. In this work, the Tabor factor was measured for each sample. The data used for comparing the nanoindentation hardness to flow stress using a Tabor factor of 2.7 comes from a convention used in Misra et al. (2005). A Tabor factor of 2.7 has shown to give a good correlation for 2D Cu/Nb, but not for 3D Cu/Nb. Tabor factors are constraint factors and will change with E/H ratio. More on the Tabor factor drop effect can be found in Gram et al. (2015). At smaller h', Tabor factors are suppressed (2.1 – 2.3), indicating that interfaces contribute to stress delocalization, making indentation hardness an unreliable proxy for true flow stress. As h' increases, the Tabor factor climbs back toward bulk-like values, reinforcing the idea that 3DIs push deformation mechanisms away from conventional nanolaminate behavior.

For example, in 3D Cu/Nb nanolaminates, shear bands broaden instead of multiplying like in traditional metallic glasses, where shear localization is abrupt and catastrophic, leading to premature failure. However, 3D Cu/Nb allows for higher deformability at sustained strengths. This is evident when comparing 10-10 Cu/Nb to 40-10 Cu/Nb. The former exhibits wide, gradual shear bands that redistribute strain effectively, while the latter shows sharp, localized bands that resemble bulk Cu/Nb behavior. At the other extreme, 10-40 Cu/Nb demonstrates a striking similarity to metallic glass deformation, but retains substantial plasticity, demonstrating that metallic glass-like behavior and high ductility can be reconciled. This insight suggests a new strategy for materials design: instead of suppressing shear localization, it is possible to modulate the quantity and thickness of shear bands through design. This strongly suggests that interfaces can be engineered to direct deformation at high strengths.

The micropillar results in Fig. 6 enable comparison between 2D and 3D Cu/Nb flow stress, as shown in Fig. 15(a). The 2.7 Tabor factor is likely to be an overestimation as these Cu/Nb systems are high-strength nanolaminates. Fig. 15(b) reflects finite element (FE) predictions of Tabor factors to decrease as the elastic ratio $E/\sigma_{8\%}$ (where E is the composite elastic modulus) drops under 100 for a nanolaminates with significant mismatch of flow strength at 8% plastic strain $\sigma_{8\%_A}/\sigma_{8\%_B}$ among its pure constituents for reference, the Cu/Ni system in Gram et al. (2015) has a $\sigma_{8\%_{Ni}}/\sigma_{8\%_{Cu}} = 2{-}3$ based on nanocrystalline Cu from Sanders et al. (1997) and nanocrystalline Ni (Detor and Schuh, 2007), while experimentally, the Cu/Nb nanolaminates in this work have $\sigma_{8\%_{Nb}}/\sigma_{8\%_{Cu}} = 1-2$ based on nanocrystalline Nb (Meyers et al., 2006) and Cu from Sanders et al. (1997). The elastic ratio of Cu/Nb as predicted by FE modeling in Hernot et al. (2014) suggest that 10-10 Cu/Nb should show an elastic modulus-to-yield strength ratio $E/\sigma_y \approx 70$, and an indentation strain $\varepsilon_i = 10 - 16\%$, resulting in a Tabor factor of 2.3–2.7. Given uncertainties in FE modeling and variations in nanocrystalline experiments depending on microstructure and strain rate, in this work, $\varepsilon_i = 8\%$ and a Tabor factor of 2.7 are assumed for indentation-to-uniaxial compression conversion, although alternative values may yield more precise correlations. Under the assumed Tabor factor and indentation strain, 3D Cu/Nb exhibits higher $\sigma_{8\%}$ than 2D Cu/Nb for $h < 80$ nm. The flow stress of 3D Cu/Nb saturates at approximately 2700 MPa for 40-10 Cu/Nb.

In contrast, previous studies (Misra et al., 2005) show that 2D Cu/Nb attains a peak indentation-correlated $\sigma_{8\%}$ of 2600 MPa at $h = 1.2$ nm. This suggests that while 3DIs are present, even though they do not inherently increase the absolute peak stress of Cu/Nb, they enable high flow stress at larger pure layer thicknesses compared to 2D architectures.

Fig. 16 presents Tabor factors for all samples in this work, calculated by dividing the hardness (H) values obtained through nanoindentation. Tabor factors are generally consistent across all samples, ranging from 1.90 to 2.16, except for 80-10 Cu/Nb, which exhibits a significantly higher Tabor factor of 2.80. 80-10 Cu/Nb behaves similarly to conventional engineering alloys when comparing hardness to uniaxial flow stress. For reference, a Tabor factor of 2.7 corresponding to an indentation strain (ε_i) of 2%–5% has been reported for 2D Cu/Nb with $h = 40$ and 5 nm (Mara et al., 2010, 2008). The deviation in Tabor factors for the other 3D Cu/Nb samples indicates that the presence of 3DIs alters yield stress (σ_y) and strain hardening exponent (n) sufficiently to invalidate the commonly assumed Tabor factor range of 2.7–3 for $\varepsilon_i = 8\%$. Recalculating the Tabor factor for 10-10 Cu/Nb using true stress-corrected values from prior work yields a value of 2.3.

Computational modeling further supports this perspective. PFDD simulations on the Cu/Nb 3DI system showed a definite increase in critical stress for slip transfer relative to their 2D counterparts. The critical stresses found in simulation range from one to three

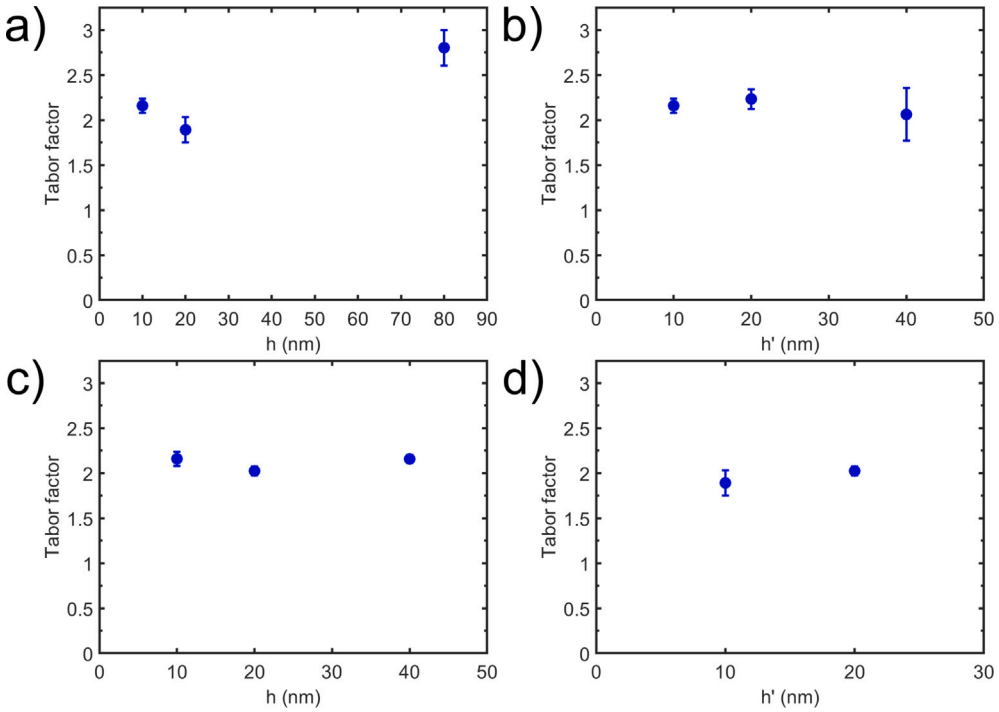

Fig. 16. Experimental Tabor factors for nanolaminates with constants (a) $h' = 10$ nm, (b) $h = 10$ nm, (c) $h/h' = 1$, and (d) $h = 20$ nm. Error bars represent a one standard deviation obtained from a Taylor series approximation of the Tabor relationship assuming zero covariance between hardness and flow stress (Lee and Forthofer, 2005). For the 40–10 sample, the flow-stress standard deviation is zero due to a sample size of one (Chen et al., 2020b).

GPA, similarly to the flow stresses seen in experiment. Furthermore, a saturation h' of 20 nm for strengthening of the 3DI was determined and changes in critical stress for slip transfer once the 3DI was established were minimal. This saturation stress of 20 nm supports the relative stability of flow strength to variations in the 3DI thickness when $h + h' \leq 50$ nm. Future work could probe smaller length scales of h and h' to see how the energetics are modified even with the introduction of a very thin 3DI.

4.2. Sub critical states

Following Xu et al. (2022a,c), we also studied the sub-critical configurations, i.e., the dislocation location when the RSS is slightly lower than the critical stress. It is found that when the dislocation moves from Cu to Nb, it arrests at the boundary between $Cu_{0.1}Nb_{0.9}$ and $Cu_{0.8}Nb_{0.2}$. However, when the dislocation moves in the opposite direction from Nb to Cu, it arrests at the boundary between Nb and $Cu_{0.1}Nb_{0.9}$. These sites correspond to locations where the relative USFE values increase. As seen in Table 1. $Cu_{0.1}Nb_{0.9}$ has the highest USFE, followed by Nb, then Cu, and lastly $Cu_{0.8}Nb_{0.2}$. When the dislocation is initiated in Nb, the largest increase relative to the USFE of Nb is at the first interface, between Nb and $Cu_{0.1}Nb_{0.9}$. On the other hand, when the dislocation is initiated in Cu, the largest increase relative to the USFE of Cu is moving from $Cu_{0.8}Nb_{0.2}$ to $Cu_{0.1}Nb_{0.9}$. Thus, in both cases, the location of the greatest increment in USFE dictates the sub-critical configuration of the dislocation.

The sub-critical configurations for the cases with amorphous precipitates are also investigated. When the dislocation originates in Cu, the dislocation stops in the middle of the 3DI, which is the same position as the case without the amorphous precipitates. However, the amorphous particles are obstacles that the dislocation must bow around. The combined effects of impenetrable obstacles at the same position where there is a large increase in USFE, (between $Cu_{0.8}Nb_{0.2}$ to $Cu_{0.1}Nb_{0.9}$) lead to an even greater increase in critical stress between $0.017\mu_{Nb}$ and $0.02175\mu_{Nb}$ than without the precipitates. On the other hand, when the dislocation originates in Nb, the subcritical configuration has changed with the introduction of the precipitate and coincides with when the dislocation first intersects the amorphous precipitate in the $Cu_{0.1}Nb_{0.9}$ layer. Here, the two energy barriers the dislocation must overcome are the increase in USFE moving from Nb to $Cu_{0.1}Nb_{0.9}$ and bowing around the amorphous precipitates. Since these do not occur at the same position, the increase in critical stress relative to the case without precipitates ranges from $0.005\mu_{Nb}$ to $0.008\mu_{Nb}$, less than half that of when the dislocations originate in Cu.

In this study, dislocations in both Cu and Nb are undissociated. Cu is FCC and is typically dissociated. Previous PFDD work on this system (Xu et al., 2022a) determined that as long as the 3D interface thickness is much thicker than the core width of the extended Cu dislocation, the dissociated nature of the dislocation core did not impact the critical stress. For Cu, the width is 11b (2.8 nm), which is smaller than the minimum 3DI thickness tested here of 10 nm.

4.3. Asymmetry in slip transmission stress

The asymmetry ratio close to 1 for $h' = 10$ nm implies that codeformation is more feasible with smaller values of h', which corresponds with the higher ductility seen in experiments for these cases (Cheng et al., 2022). When pileups are present, there is a greater degree of asymmetry in slip transfer. This supports the theory that larger pileups can induce anisotropic slip and eventual shear banding, indicating once again that the effect of 3DIs is dependent on their thickness (Cheng et al., 2022).

The simulations suggest that 3D interfaces can minimize the slip transfer asymmetry compared to the 2D cases. Nearly equivalent slip strengths in both directions can aid in co-deformation and uniform deformation across the composite. Applying the hypothesis that slip transfer asymmetry indicates a lower propensity for codeformability implies that the low slip transfer asymmetry for the amorphous cases correlates well with the micropillar results for 10–40 Cu/Nb, which has moderate deformability. The asymmetry in slip transfer seen across all the simulations implies that 3DI thickness is a microstructural feature that can affect other mechanical properties than just the overall strength (Cheng et al., 2024).

4.4. Extensions to other systems

The broader implications of these findings extend beyond Cu/Nb nanolaminates. Ultimately, this work quantifies h and h′ windows in Cu/Nb and suggests design principles; extension to other systems requires system-specific validation, demonstrating that high-strength materials do not have to be concomitantly less ductile. By broadening rather than suppressing shear bands, we can harness the very mechanisms that limit conventional nanolaminates and transform them into pathways for enhanced performance. This represents a fundamental shift in how interfaces are conceptualized and designed, diverging from the view that interfaces only bear properties that are solely consequences of the chemical and structural properties of the adjoining phases. Altering some properties of the interface, such as thickness, independently from the neighboring phases opens another way for designing materials that are not only exceptionally strong but more resistant to catastrophic failure under extreme conditions. This approach could be extended to other FCC/BCC nanolaminates and engineered to optimize performance in extreme environments, from aerospace applications to next-generation wear-resistant coatings.

4.5. Future work

There is still more to be investigated from a simulation standpoint with regard to the improvements in ductility brought about by the introduction of a 3D interface. PFDD provides insight into a deformation mechanism underlying experimental measurements of strength and qualitative comparison between critical stresses for slip transfer and macro scale strength. On the one side, the model does not use any adjustable parameters. However, on the other side, it is a mesoscale model and the thermodynamics of slip are not taken into account, limiting its ability to predict stress strain responses. Modeling techniques such as the Slip band Crystal Plasticity Fast-Fourier Transform method (SB-FFT), however, could be used to investigate slip band transmission variation between 2D and 3D interfaces and with stronger connection with experiment strength values (Ahmadikia et al., 2023). Further, these simulations can take into account lattice rotation and simulate slip bands on differing slip systems and forecast stress–strain behavior (Ahmadikia et al., 2021), which would align well with the shear banding seen in experiment. The CP-FFT technique microstructure sensitive micro mechanical models, which allows investigation of the effects of relative layer thicknesses h and h'.

Conclusions

In this work, we studied the strength and failure response of Cu/Nb nanolaminates containing thick interfaces, referred to as 3D interfaces (3DIs). Of particular focus was the role of the individual layer thickness h and 3DI thickness h', which has not been studied to date. To this end, Cu/Nb nanolaminates of varying h were synthesized with conventional sharp (2D) and 3DIs of varying thicknesses h'. We also developed a dislocation dynamics model to simulate dislocation transmission across these interfaces and to estimate the critical stress required for transmission in both slip directions.

Key conclusions from this study include:

- 3DIs further enhance the strength Cu/Nb nanolaminates for the same h and drastically reduce the size effect of h on strength.
- Shear band formation in 3DI nanolaminates is delocalized, under a critical thickness h'_{crit}, in which broad shear bands form, allowing for sustained plasticity. This response is distinct from the concentrated shear banding and brittle failure in 2D nanolaminates with sharp interfaces ($h' = 0$) and metallic glasses (e.g., $\approx h' = \infty$).
- The Tabor factor evolves with interface structure, indicating that conventional hardness-to-strength correlations may not apply to nanolaminates with 3DIs.
- Slip transfer across the Cu/Nb is asymmetric, favoring strengthening in Cu more than Nb. 3DIs alter the asymmetry and certain thicknesses can reduce it, a finding that can be leveraged in future material designs.
- A critical length-scale regime ($(h + h') \leq 50$ nm) exists where 3DIs maximize both strength and deformability, while larger h' values push the system toward metallic-glass-like behavior.

CRediT authorship contribution statement

Mauricio De Leo: Writing – review & editing, Writing – original draft, Visualization, Formal analysis, Data curation, Conceptualization. **Nicolas Fuchs-Lynch:** Writing – review & editing, Writing – original draft, Visualization, Formal analysis, Data curation, Conceptualization. **Justin Y. Cheng:** Investigation, Formal analysis, Data curation, Conceptualization. **Shuozhi Xu:** Investigation, Formal analysis, Data curation, Conceptualization. **Irene J. Beyerlein:** Writing – review & editing, Validation, Supervision, Resources, Project administration, Methodology, Funding acquisition, Formal analysis, Data curation, Conceptualization. **Nathan A. Mara:** Writing – review & editing, Validation, Supervision, Resources, Project administration, Methodology, Funding acquisition, Formal analysis, Data curation, Conceptualization.

Declaration of competing interest

The authors declare that they have no known competing financial interests or personal relationships that could have appeared to influence the work reported in this paper.

Acknowledgments

The authors acknowledge financial support from the Department of Energy, Office of Science, Basic Energy Sciences Program DE-SC0020133. Use was made of computational facilities purchased with funds from the National Science Foundation, United States (CNS-1725797) and administered by the Center for Scientific Computing (CSC). The CSC is supported by the California NanoSystems Institute and the Materials Research Science and Engineering Center (MRSEC; NSF DMR 2308708) at UC Santa Barbara. Access to the University of Minnesota's Characterization Facility for FIB/SEM, TEM and nanoindentation testing is gratefully acknowledged. This work was performed, in part, at the Center for Integrated Nanotechnologies, an Office of Science User Facility operated for the U.S. Department of Energy (DOE) Office of Science by Los Alamos National Laboratory (Contract 89233218CNA000001) and Sandia National Laboratories (Contract DE-NA-0003525).

Appendix A. Supplementary data

Supplementary material related to this article can be found online at https://doi.org/10.1016/j.ijplas.2026.104640.

Data availability

Data will be made available on request.

References

Ahmadikia, B., Kumar, M.A., Beyerlein, I.J., 2021. Effect of neighboring grain orientation on strain localization in slip bands in HCP materials. Int. J. Plast. 144, 103026.

Ahmadikia, B., Wang, L., Kumar, M.A., Beyerlein, I.J., 2023. Grain boundary slip–twin transmission in titanium. Acta Mater. 244, 118556.

Beyerlein, I.J., Hunter, A., 2016. Understanding dislocation mechanics at the mesoscale using phase field dislocation dynamics. Philos. Trans. R. Soc. A 374 (2066), 20150166.

Beyerlein, I.J., Li, Z., Mara, N.A., 2022. Mechanical properties of metal nanolaminates. Annu. Rev. Mater. Res. 52 (1), 281–304.

Cao, Z., Cai, Y., Sun, C., Ma, Y., Wei, M., Li, Q., Lu, H., Wang, H., Zhang, X., Meng, X., 2019. Tailoring strength and plasticity of Ag/Nb nanolaminates via intrinsic microstructure and extrinsic dimension. Int. J. Plast. 113, 145–157.

Chen, Y., Li, N., Hoagland, R.G., Liu, X.-Y., Baldwin, J., Beyerlein, I.J., Cheng, J., Mara, N., 2020b. Effects of three-dimensional Cu/Nb interfaces on strengthening and shear banding in nanoscale metallic multilayers. Acta Mater. 199, 593–601.

Chen, H., Zhao, Y., Zhang, J., Wang, Y., Li, G., Wu, K., Liu, G., Sun, J., 2020a. He-ion irradiation effects on the microstructure stability and size-dependent mechanical behavior of high entropy alloy/cu nanotwinned nanolaminates. Int. J. Plast. 133, 102839.

Cheng, J.Y., Wang, J., Chen, Y., Xu, S., Barriocanal, J.G., Baldwin, J.K., Beyerlein, I.J., Mara, N.A., 2024. 3D interfaces enhance nanolaminate strength and deformability in multiple loading orientations. Acta Mater. 267, 119697.

Cheng, J.Y., Xu, S., Chen, Y., Li, Z., Baldwin, J.K., Beyerlein, I.J., Mara, N.A., 2022. Simultaneous high-strength and deformable nanolaminates with thick biphase interfaces. Nano Lett. 22 (5), 1897–1904.

Demkowicz, M.J., Beyerlein, I.J., 2020. The effects of nanoscale confinement on the behavior of metal laminates. Scr. Mater. 187, 130–136. http://dx.doi.org/10.1016/j.scriptamat.2020.05.057, URL: https://www.sciencedirect.com/science/article/pii/S1359646220303456.

Detor, A.J., Schuh, C.A., 2007. Tailoring and patterning the grain size of nanocrystalline alloys. Acta Mater. 55 (1), 371–379.

Ebrahimi, M., Luo, B., Wang, Q., Attarilar, S., 2024. High-performance nanoscale metallic multilayer composites: Techniques, mechanical properties and applications. Materials 17 (9), 2124.

Eshelby, J.D., 1957. The determination of the elastic field of an ellipsoidal inclusion, and related problems. Proc. R. Soc. Lond. Ser. A 241 (1226), 376–396.

Geng, C., Huang, B., Zhang, N., Yi, J., Wang, Q., Jia, Y., Li, F., Luan, J., Hou, X., Huang, W., et al., 2022. Evolution of local densities during shear banding in Zr-based metallic glass micropillars. Acta Mater. 235, 118068.

Gola, A., Zhang, G.-P., Pastewka, L., Schwaiger, R., 2019. Surface flaws control strain localization in the deformation of Cu | Au nanolaminate pillars. MRS Commun. 9 (3), 1067–1071.

Gram, M.D., Carpenter, J.S., Anderson, P.M., 2015. An indentation-based method to determine constituent strengths within nanolayered composites. Acta Mater. 92, 255–264.

Hattar, K., Demkowicz, M., Misra, A., Robertson, I., Hoagland, R., 2008. Arrest of He bubble growth in Cu–Nb multilayer nanocomposites. Scr. Mater. 58 (7), 541–544.

Hernot, X., Moussa, C., Bartier, O., 2014. Study of the concept of representative strain and constraint factor introduced by Vickers indentation. Mech. Mater. 68, 1–14.
Hirsch, P.B., Kelly, A., 1965. Stacking-fault strengthening. Philos. Mag. 12 (119), 881–900.
Hoagland, R., Mitchell, T., Hirth, J., Kung, H., 2002. On the strengthening effects of interfaces in multilayer fee metallic composites. Phil. Mag. A 82 (4), 643–664.
Hunter, A., Leu, B., Beyerlein, I.J., 2018. A review of slip transfer: applications of mesoscale techniques. J. Mater. Sci. 53, 5584–5603.
Jiang, L., Chawla, N., 2010. Mechanical properties of Cu6Sn5 intermetallic by micropillar compression testing. Scr. Mater. 63 (5), 480–483.
Koehler, J., 1970. Attempt to design a strong solid. Phys. Rev. B 2 (2), 547.
Lee, E.S., Forthofer, R.N., 2005. Analyzing Complex Survey Data. Sage Publications.
Lei, L., Marin, J.L., Koslowski, M., 2013. Phase-field modeling of defect nucleation and propagation in domains with material inhomogeneities. Modelling Simul. Mater. Sci. Eng. 21 (2), 025009.
Li, Z., Cheng, J.Y., Poplawsky, J.D., Xu, S., Baldwin, J.K., Beyerlein, I.J., Mara, N.A., 2023. Critical length scales for chemical heterogeneity at Cu/Nb 3D interfaces by atom probe tomography. Scr. Mater. 223, 115078.
Li, S.-H., Li, J.-T., Han, W.-Z., 2019. Radiation-induced helium bubbles in metals. Materials 12 (7), 1036.
Lim, L., Raj, R., 1985. Continuity of slip screw and mixed crystal dislocations across bicrystals of nickel at 573 K. Acta Metall. 33 (8), 1577–1583.
Mara, N., Bhattacharyya, D., Dickerson, P., Hoagland, R., Misra, A., 2008. Deformability of ultrahigh strength 5 nm Cu / Nb nanolayered composites. Appl. Phys. Lett. 92 (23).
Mara, N., Bhattacharyya, D., Hirth, J., Dickerson, P., Misra, A., 2010. Mechanism for shear banding in nanolayered composites. Appl. Phys. Lett. 97 (2).
Meyers, M.A., Mishra, A., Benson, D.J., 2006. Mechanical properties of nanocrystalline materials. Prog. Mater. Sci. 51 (4), 427–556.
Mianroodi, J.R., Svendsen, B., 2015. Atomistically determined phase-field modeling of dislocation dissociation, stacking fault formation, dislocation slip, and reactions in fcc systems. J. Mech. Phys. Solids 77, 109–122.
Misra, A., Hirth, J., Hoagland, R., 2005. Length-scale-dependent deformation mechanisms in incoherent metallic multilayered composites. Acta Mater. 53 (18), 4817–4824.
Nasim, M., Li, Y., Wen, M., Wen, C., 2020. A review of high-strength nanolaminates and evaluation of their properties. J. Mater. Sci. Technol. 50, 215–244.
Nizolek, T., Begley, M., McCabe, R., Avallone, J., Mara, N., Beyerlein, I., Pollock, T., 2017. Strain fields induced by kink band propagation in Cu-Nb nanolaminate composites. Acta Mater. 133, 303–315.
Pathak, S., Velisavljevic, N., Baldwin, J.K., Jain, M., Zheng, S., Mara, N.A., Beyerlein, I.J., 2017. Strong, ductile, and thermally stable bcc-Mg nanolaminates. Sci. Rep. 7 (1), 8264.
Qiu, X., Tang, R., Liu, R., Huang, H., Guo, S., Yu, H., 2012. A micro initiator realized by reactive Ni/Al nanolaminates. J. Mater. Sci., Mater. Electron. 23 (12), 2140–2144.
Rao, S., Hazzledine, P., 2000. Atomistic simulations of dislocation–interface interactions in the Cu-Ni multilayer system. Phil. Mag. A 80 (9), 2011–2040.
Roach, A.M., Xu, S., Luscher, D.J., Gianola, D.S., Beyerlein, I.J., 2023. Interaction of extended dislocations with nanovoid clusters. Int. J. Plast. 168, 103684.
Sáenz-Trevizo, A., Hodge, A., 2020. Nanomaterials by design: a review of nanoscale metallic multilayers. Nanotechnology 31 (29), 292002.
Sanders, P.G., Eastman, J., Weertman, J., 1997. Elastic and tensile behavior of nanocrystalline copper and palladium. Acta Mater. 45 (10), 4019–4025.
Selimov, A., Chu, K., McDowell, D., 2022. Effects of interdiffusion on shear response of semi-coherent {111} interfaces in Ni/Cu. Int. J. Plast. 157, 103393.
Sim, G.-D., Krogstad, J.A., Reddy, K.M., Xie, K.Y., Valentino, G.M., Weihs, T.P., Hemker, K.J., 2017. Nanotwinned metal MEMS films with unprecedented strength and stability. Sci. Adv. 3 (6), e1700685.
Singh, M., Jonnalagadda, K., 2024. An in-situ investigation of the strain partitioning and failure across the layers in a multi-layered steel. Exp. Mech. 64 (5), 703–727.
Wang, Y., Li, J., 2010. Phase field modeling of defects and deformation. Acta Mater. 58 (4), 1212–1235.
Wang, J., Misra, A., 2011. An overview of interface-dominated deformation mechanisms in metallic multilayers. Curr. Opin. Solid State Mater. Sci. 15 (1), 20–28.
Wang, J., Zhou, Q., Shao, S., Misra, A., 2017. Strength and plasticity of nanolaminated materials. Mater. Res. Lett. 5 (1), 1–19.
Warlimont, H., Martienssen, W., 2018. Springer Handbook of Materials Data. Springer.
Xu, S., Cheng, J.Y., Li, Z., Mara, N.A., Beyerlein, I.J., 2022b. Phase-field modeling of the interactions between an edge dislocation and an array of obstacles. Comput. Methods Appl. Mech. Engrg. 389, 114426.
Xu, S., Cheng, J., Mara, N., Beyerlein, I.J., 2022a. Thick interface size effect on dislocation transmission in nanolaminates. In: IOP Conference Series: Materials Science and Engineering. vol. 1249, IOP Publishing, 012005.
Xu, S., Cheng, J.Y., Mara, N.A., Beyerlein, I.J., 2022c. Dislocation dynamics in heterogeneous nanostructured materials. J. Mech. Phys. Solids 168, 105031. http://dx.doi.org/10.1016/j.jmps.2022.105031, URL: https://www.sciencedirect.com/science/article/pii/S0022509622002083.
Xu, S., Hwang, E., Jian, W.-R., Su, Y., Beyerlein, I.J., 2020a. Atomistic calculations of the generalized stacking fault energies in two refractory multi-principal element alloys. Intermetallics 124, 106844.
Xu, S., Mianroodi, J.R., Hunter, A., Svendsen, B., Beyerlein, I.J., 2020b. Comparative modeling of the disregistry and Peierls stress for dissociated edge and screw dislocations in Al. Int. J. Plast. 129, 102689.
Xu, S., Smith, L., Mianroodi, J.R., Hunter, A., Svendsen, B., Beyerlein, I.J., 2019. A comparison of different continuum approaches in modeling mixed-type dislocations in Al. Modelling Simul. Mater. Sci. Eng. 27 (7), 074004.
Xu, S., Su, Y., Smith, L.T., Beyerlein, I.J., 2020. Frank-read source operation in six body-centered cubic refractory metals. J. Mech. Phys. Solids 141, 104017.
Yang, L., Mayer, C., Chawla, N., LLorca, J., Molina-Aldareguía, J., 2020. Nanomechanical characterization of the fracture toughness of Al/SiC nanolaminates. Extrem. Mech. Lett. 40, 100945.
Yang, Y., Ye, J., Lu, J., Gao, Y., Liaw, P.K., 2010. Metallic glasses: gaining plasticity for microsystems. Jom 62, 93–98.
Ye, C., Ge, S., Zou, B., Wang, Y.M., Zhang, D., Ding, J., Wang, K., Li, Z., 2025. Atomic-scale deformation mechanisms in metal nanocomposites with intragranular amorphous nanoparticles. Int. J. Plast. 104398.
Ye, J., Lu, J., Yang, Y., Liaw, P., 2009. Study of the intrinsic ductile to brittle transition mechanism of metallic glasses. Acta Mater. 57 (20), 6037–6046.
Zeng, Y., Cai, X., Koslowski, M., 2019. Effects of the stacking fault energy fluctuations on the strengthening of alloys. Acta Mater. 164, 1–11.
Zeng, Y., Hunter, A., Beyerlein, I.J., Koslowski, M., 2016. A phase field dislocation dynamics model for a bicrystal interface system: An investigation into dislocation slip transmission across cube-on-cube interfaces. Int. J. Plast. 79, 293–313.
Zhang, R., Germann, T., Liu, X.-Y., Wang, J., Beyerlein, I., 2014. Layer size effect on the shock compression behavior of fcc–bcc nanolaminates. Acta Mater. 79, 74–83.
Zhang, Y., He, C.-Y., Wang, X., Hama, T., Sun, B., Jia, Y.-F., Zhang, X.-C., Tu, S.-T., 2024. Revealing the fatigue strengthening and damage mechanisms of surface-nanolaminated gradient structure. Int. J. Plast. 182, 104128.
Zhang, J., Wu, K., Zhang, L., Wang, Y., Liu, G., Sun, J., 2017. Unraveling the correlation between hall-petch slope and peak hardness in metallic nanolaminates. Int. J. Plast. 96, 120–134.
Zheng, S., Wang, J., Carpenter, J., Mook, W., Dickerson, P., Mara, N., Beyerlein, I.J., 2014. Plastic instability mechanisms in bimetallic nanolayered composites. Acta Mater. 79, 282–291.